2017

Heat and Mass Transfer in a Cylindrical Heat Pipe with Idealized Porous Lining

Pramesh Regmi
Louisiana State University and Agricultural and Mechanical College, pramesh.regmi@gmail.com

HEAT AND MASS TRANSFER
IN A CYLINDRICAL HEAT PIPE WITH IDEALIZED POROUS LINING

A Thesis
Submitted to the Graduate Faculty of the
Louisiana State University and
Agricultural and Mechanical College
in partial fulfillment of the
requirements for the degree of
Master of Science
in Mechanical Engineering

in

The Department of Mechanical Engineering

by
Pramesh Regmi
B.S., McNeese State University, 2015
May 2017

ACKNOWLEDGEMENTS

First of all, the author would like to express his most sincere and deepest debt of gratitude to his major professor, Dr. Harris Wong for his constant encouragement, insightful suggestions, and patient guidance and help throughout the work. The author would also like to thank Dr. Sunggook Park and Dr. Krishnaswamy Nandakumar for their time and effort to serve on his examination committee.

The author would also like to thank his professors, colleagues and friends who have provided encouragement and discussions to enhance the understanding of the author. The author also appreciates the great time they spent together.

In addition, the author would like to thank God and his family for their constant love and support from the start. The parents of the author, Mr. Murari Regmi and Mrs. Rekha Kumari Regmi, have always supported the author and this thesis is dedicated to them. The author also wants to thank his brother Mr. Prabhakar Regmi and his sister-in-law Mrs. Samikshya Regmi for their encouragement and support.

Lastly, the author wants to thank LSU Graduate School for giving the opportunity to the author to study and complete his studies at LSU.

TABLE OF CONTENTS

LIST OF FIGURES

ABSTRACT

Many devices use heat pipes for cooling. They can be of different cross-sectional shapes and can range from 15 m long to 10 mm. In this work, the heat and mass transfer in a cylindrical heat pipe is modelled. The heat pipe is lined with a wick next to the wall. The wick consists of straight capillaries that run the whole length of the pipe and radially aligned capillaries that span the width of the wick. The capillaries are filled with a partially wetting liquid, and the center of the pipe is filled with its vapor. The radial capillaries are connected to the axial capillaries and are opened to the vapor region at the wick surface. The pipe is initially charged with an amount of liquid such that the liquid-vapor interface at the radial capillary openings is flat. When one end of the pipe is heated, the liquid evaporates and increases the vapor pressure. Hence, the vapor is driven to the cold end where it condenses and releases latent heat. The condensate moves back to the hot end through the capillaries in the wick. Steady-flow problem is solved in this work assuming a small imposed temperature difference between the two ends making the temperature profile skew-symmetric. So, we only need to focus on the heated half. Also, since the pipe is slender, the axial flow gradients are much smaller than the cross-stream gradients. Therefore, evaporative flow in a cross-sectional plane can be treated as two-dimensional. Evaporation rate in each pore is solved in the limit the evaporation number $E \to \infty$ to find that the liquid evaporates mainly in a boundary layer at the contact line. An analytical solution is obtained for the leading order evaporation rate. Therefore, we find the analytic solutions for the temperature profile and pressure distributions along the pipe. Two dimensionless numbers emerge from the momentum and energy equations: the heat pipe number, H, which is the ratio of heat transfer by vapor flow to conductive heat transfer in the liquid and wall, and the evaporation exponent, S, which controls

the evaporation gradient along the pipe. Conduction in the liquid and wall dominates in the limit $H \to 0$ and $S \to 0$. When $H \to \infty$ and $S \to \infty$, vapor-flow heat transfer dominates and a thermal boundary layer appears at the hot end whose thickness scales as $S^{-1}L$, where L is the half length of the pipe. A similar boundary layer exists at the cold end. The regions outside the boundary layer is uniform. These regions correspond to the evaporating, adiabatic and the condensing regions commonly observed in heat pipes. For fixed cross-sectional pipe configuration, we find an optimal pipe length for evaporative heat transfer. For fixed pipe length, we also find an optimal wick thickness for evaporative heat transfer. These optimal pipe length and wick thickness can help to improve the design of a heat pipe and are found for the first time.

CHAPTER 1. INTRODUCTION

A heat pipe consists of a sealed container lined with a wicking material (Peterson 1994). A liquid fills the porous lining whereas its vapor fills the rest. As one end of a heat pipe is heated, the liquid evaporates and increases the vapor pressure, which drives a vapor flow towards the cold end. There, the vapor condenses and releases the latent heat. The liquid then flows along the capillaries in the wick back to the hot end, and completes a cycle. The length of the heat pipe is divided into three sections: evaporator, adiabatic (transport) and condenser (Faghri 1995). The advantage of using a heat pipe over other conventional methods is that large quantities of heat can be transported through a small cross-sectional area over a considerable distance with no additional power input to the system (Faghri 1995). The heat transfer capacity of a heat pipe is several orders of magnitude (approximately 10^3) greater than even the best solid conductors. Also, heat pipes are simple to design and manufacture. Furthermore, heat pipes have the unique ability to control and transport high heat rates at various temperature (Peterson 1994, Faghri 1995). Only with few limitations on the manner of use, heat pipes can be regarded as synergistic engineering structure. This is a structure which is equivalent to a material having a thermal conductivity which greatly exceeds the thermal conductivity of any known metal.

All developed countries are involved in the research, development and commercialization of the heat pipes because of its high use and benefits (Faghri 2014). Heat pipes research and applications were started in many countries from 1960s (Andrews 1996). Theoretical and Experimental studies on evaporation heat transfer characteristics of goove heat pipe have been conducted by Toyokawa, et al. as well as Iwasa, et al. in Japan (Toyokawa 1993) (Iwasa 1994). Similarly, Lin (Lin 1992) studied the effects of fluid properties and axial conduction through the

pipe wall on thermal performance. His results showed that the ratio of conduction and convection inside a heat pipe is an important factor, in addition to the ratio of liquid-wick matrix radial conduction and wall axial conduction. Similarly, variable conductance heat pipe (VCHP) has been studied by Lu (Lu 1995), where he studied three kinds of VCHPs: a flat heat pipe without gas reservoir, and a circular heat pipe with non-wicked gas reservoir, both using water and methanol as working fluid and nitrogen as gas; and thirdly a heat pipe using a two-component working fluid at different concentration ratios, Water and methanol mixture was used as the working fluid.

Heat pipes are used in the following areas: aerospace, heat exchangers, electrical and electronic equipment cooling, ovens and furnaces, production tools, medicine and human body temperature control, transportation systems and deicing, engines and automotive industry, permafrost stabilization and manufacturing (Faghri 1995). Akbarzadeh (Akbarzadeh 1995) conducted research to use heat pipe for power generation. Similarly, experiments carried out by Xiao (Xiao 1995) show that the heat pipe heat exchangers can be advantageous for replacing conventional reheat coils in air conditioning systems. Also, heat pipe system to cool electronic equipment in a totally sealed cabinet has been developed. (Bandopadhayay 1992). Heat pipes have also been developed for extracting geothermal energy (Mochizuki 1994) as well as cooling of electric power cables (Mochizuki 1994). Similarly, heat pipes has been used to absorb the exhaust heat of an automobile engine (Kanesashi 1996).

The cylindrical heat pipe with porous material lining the inner wall is a type of capillary-driven heat pipe. The purpose of pores and capillaries is to provide a capillary-driven pump for returning the condensate to the evaporator section. There should be enough fluid placed in the heat pipe to saturate the pores with the liquid. If the amount of liquid is low, the heat pipe may

fail. The basic working principle for the capillary-driven heat pipe is the same as a conventional heat pipe (Reay 2014). The capillaries help the condensate flow from the cold end to the hot end. Due to the two-phase nature of the capillary heat pipe, it is ideal for transferring heat over long distance with a very small temperature drop, and for creating a nearly isothermal surface for temperature stabilization (Faghri, 1995).The most common limitation for this type of heat pipe is the capillary limit which occurs when the capillaries cannot return enough liquid to the evaporator section which results in sudden and continuous rise in the evaporator wall temperature. There are other constraints, such as sonic and vapor pressure limits (Faghri 2012).

Previously, heat pipes have been studied starting from the difference in pressure between the liquid and the vapor side of the interface. While doing so, the capillary pressure is calculated assuming constant interfacial curvature at all the pores which depend on the radius of the pore for cylindrical case. The liquid pressure drop was successfully calculated in previous models (Chi 1976). However, there were difficulties in evaluating the vapor pressure gradient (Chi 1976). This was because the kinetics of vapor evaporation and condensation were not considered in the previous models (Dunn 1982).

This paper has resolved the above-mentioned issues. Starting from the study of evaporation in the pore, we successfully computed the vapor pressure along the pipe, as shown in Section 8. In addition, using the vapor pressure and the liquid pressure along the axial direction of the pipe, we were able to predict the interfacial curvature that varies along the pipe (Section 10). Also, comparing with the previous work done, our approach does not require heat flux to calculate the heat transfer in a heat pipe. The prescribed wall temperature is sufficient. This is a more convenient approach as it is easier to measure the temperature then knowing the heat flux.

CHAPTER 2. A MODEL HEAT PIPE

Figures 1(a) and (b) show cross sections of the circular cylindrical heat pipe of outer wall radius R_o and length 2L. The vapor moves along the center of the pipe in a circular channel of radius R_g. The wick occupies the region between the vapor and the inner pipe wall at radius R_i, and is made of a solid material with liquid-filled circular capillaries that run from one end of the pipe to the other. These capillaries have the same radius R_p. There are N_r and N_θ capillaries evenly spaced in the radial and circumferential directions, respectively, as shown in Figure 1(a). There are also liquid-filled capillaries that run radially from the vapor region to the inner pipe wall (Figure 1(b)). These capillaries are open to the vapor region and closed at the pipe surface, and are connected to the axially aligned capillaries. There are N_θ radially running capillaries arranged on an axial cross-sectional plane, and there are $2N_z$ evenly spaced planes in the axial direction. Hence, there are totally $2N_\theta N_z$ radial capillaries that connect the axial capillaries to the vapor region.

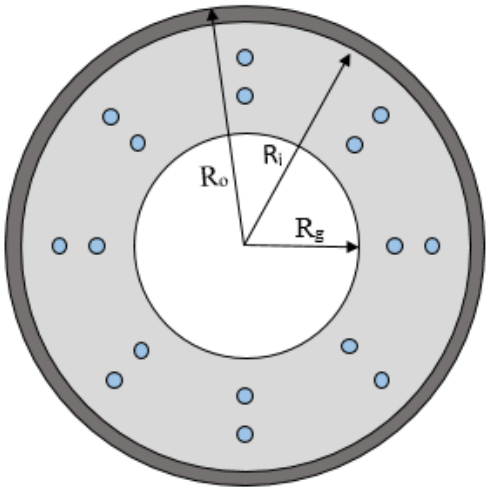

Figure 1 (a). An axial cross section showing the circular vapor region at the center surrounded by the wick with liquid-filled capillaries, all fitted inside the pipe wall. There are N_r and N_θ capillaries evenly spaced in the radial and circumferential directions, respectively. For the pipe shown, $N_r = 2$ and $N_\theta = 8$.

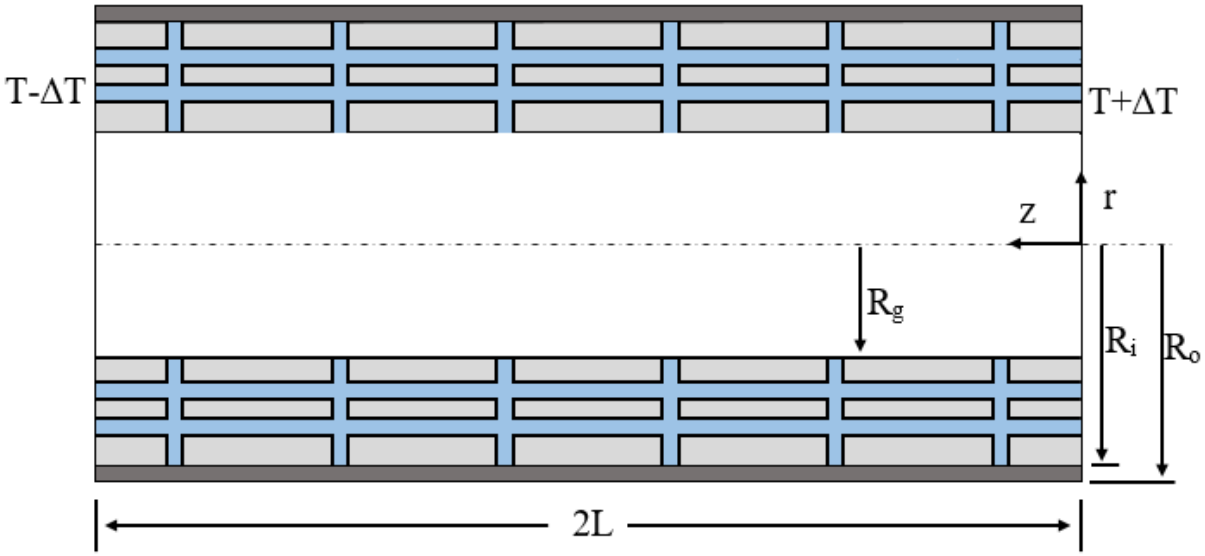

Figure 1. (b) A longitudinal cross section along the mid plane of the pipe. It shows the liquid-filled radial capillaries connecting the axial capillaries. A cylindrical coordinate system is defined at the hot end. There are N_θ radial capillaries on a cross-sectional plane at constant z, and $2N_z$ evenly spaced planes along the length of the pipe. For the pipe shown, N_z=3.

Initially, the temperature of the pipe is maintained at T_0. The axial and radial capillaries are filled with a liquid and the center circular channel is filled with its vapor. The amount of liquid charged is controlled to give a planar liquid-vapor interface at the pores. The liquid is assumed to partially wet the wick material so that the interface is pinned at the pore edge for small deflections of the interface. The liquid is at temperature T_0, and the vapor is at the corresponding equilibrium pressure P_0. One end of the pipe is then heated to $T_0+\Delta T$, and the other end is cooled to $T_0-\Delta T$. These end temperatures are maintained and the heat pipe reaches a steady state. The outer surface of the heat pipe is insulated. The equilibrium vapor pressure at the higher-temperature end is greater than the equilibrium vapor pressure at the lower-temperature end. This results in a vapor pressure gradient that drives the vapor from the hot end towards the cold end. After the vapor moves away from the hot end, the vapor pressure at the hot end drops below the local equilibrium vapor pressure which induces continuous evaporation. As a result, the interface curves towards

the liquid side. At the cold end, the incoming vapor flow increases the vapor pressure to be higher than the local equilibrium vapor pressure. This results in continuous condensation at the cold end that increases the liquid volume and raises the interface. The difference in interfacial curvature between the hot and cold ends generates a liquid pressure gradient that drives the liquid from the cold end back to the hot end along the porous lining. In the next section, we study the evaporation kinetics to determine the local evaporative mass flux at the interface.

CHAPTER 3. EVAPORATION IN A PORE

The temperature distribution along the pipe will be skew symmetric owing to the small temperature difference across the pipe. Thus, we will focus on the heated half of the pipe. Furthermore, the axial pore spacing is assumed small compared with the length of the heat pipe. Thus, the temperature and pressure variations along the pipe occur over length scales that are much larger than the pore spacing. Hence, locally at a pore, the pipe temperature and vapor pressure can be taken as constant. The mass evaporation rate at a pore will be analyzed in this section.

3.1 Governing Equations for Evaporation

Figure 2 shows a typical radially aligned capillary and its opening to the vapor region. The local pipe wall temperature surrounding the channel is T_p, and the equilibrium vapor pressure corresponding to this temperature is p_e. As vapor flows away from the heated half of the pipe, the vapor pressure p_g above the pore drops below p_e. This induces continuous evaporation at the liquid-vapor interface.

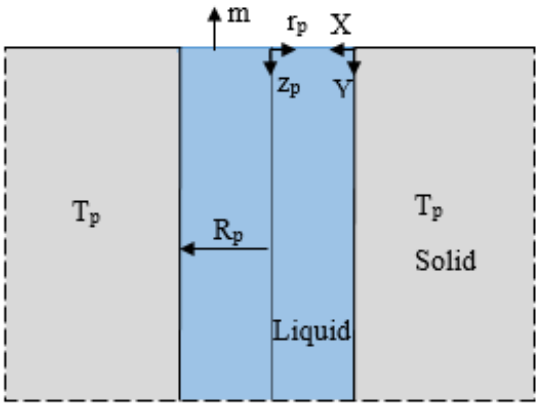

Figure 2. A cross section of a liquid-filled circular pore of radius R_p. The liquid-vapor interface is planar with a coordinate system (r_p, z_p) defined at the center. A local coordinate system (X,Y) is defined at the contact line to resolve the inner temperature profile.

The evaporative mass flux at a point on the interface is proportional to the difference between the equilibrium vapor pressure and p_g:

$$m = c(p_i - p_g); \qquad c = \frac{\alpha}{\sqrt{2\pi R_s T_p}}, \tag{3.1}$$

where p_i is the equilibrium vapor pressure corresponding to the local interface temperature T_i, α is the accommodation coefficient, R_s is the specific gas constant, and the parameter c is inversely proportional to the speed of sound in vapor. The local evaporative mass flux m is positive for evaporation and negative for condensation. This equation is derived from a kinetic theory and it conserves momentum and energy at the interface whereas some other commonly used forms do not (Barrett, 1992). Since $p_i = p_i(T_i)$ and the change in pressure from p_g to p_i is small, we can expand p_i about p_g as

$$p_i = p_g + \frac{dp_i}{dT_i}(T_i - T_g) + ..., \tag{3.2}$$

where T_g is the saturation temperature at pressure p_g. Also, since the function $p_i = p_i(T_i)$ relates the saturation pressure to temperature, the gradient dp_i/dT_i can be evaluated using the Clapeyron equation (Kenneth 1988) as

$$\frac{dp_i}{dT_i} = \frac{\rho_e h_{fg}}{T_p}, \tag{3.3}$$

where ρ_e is the equilibrium vapor density, and h_{fg} is the latent heat of vaporization of the working fluid, both evaluated at temperature T_p. Although the gradient should be evaluated at temperature T_g, we use T_p because it is a boundary condition and $|T_p - T_g| << T_p$. The evaporative mass flux then becomes

$$m = \frac{c\rho_e h_{fg}(T_i - T_g)}{T_p} \tag{3.4}$$

Therefore, the interfacial evaporative mass flux m = m(T_i), which will serve as a boundary condition for the liquid temperature.

Owing to the small size of the pore, convective heat transfer in the liquid is negligible, and the liquid temperature obeys

$$\nabla^2 T = 0\,, \tag{3.5}$$

where ∇^2 is the axisymmetric Laplacian operator because the capillary is circular and the liquid temperature inside is axisymmetric. This governing equation is subject to the following boundary conditions. At the liquid-vapor interface z_p=0, an energy balance gives that the evaporative heat flux is supplied by the conductive heat flux in the liquid

$$mh_{fg} = k_f \frac{dT}{dz_p} \tag{3.5a}$$

Here, k_f is the liquid thermal conductivity, and a local cylindrical coordinate system (r_p,z_p) is defined as shown in Figure 2. The interface is taken to be planar because of the assumption that the system deviates infinitesimally from the initial equilibrium configuration. At the capillary wall r_p=R_p, the liquid temperature is the same as the local pipe temperature

$$T = T_p\,. \tag{3.5b}$$

Since the capillary radius R_p is small compared with the pipe radius R_o, the liquid temperature T inside the capillary will asymptote to the wall temperature T_p within a distance $z_p \sim R_p << R_i$. Hence, we can take the radial channel length to be infinity for the liquid temperature calculation, and as $z_p \to \infty$,

$$T \to T_p. \tag{3.5b}$$

Thus, the liquid temperature T inside the pore can be solved. Solution of (3.5) yields the interface temperature T_i=T_i(r_p). This allows the mass evaporation rate at a pore to be calculated as

$$M_p = \int_0^{R_p} 2\pi r_p m dr_p \,. \tag{3.6}$$

The purpose of this section is to find M_p.

3.2 Non-dimensionalization

We define a set of dimensionless variables:

$$r_p^* = \frac{r_p}{R_p},\quad z_p^* = \frac{z_p}{R_p},\quad T^* = \frac{T - T_g}{T_p - T_g},\quad M_p^* = \frac{M_p}{2\pi R_p^2 c\rho_e h_{fg}(T_p - T_g)/T_p} \tag{3.7 a, b, c, d}$$

The governing equation (3.5a) becomes

$$\nabla^{*2} T^* = 0 \tag{3.8}$$

At the interface, $z_p^*=0$,

$$T^* = E^{-1}\frac{dT^*}{dz_p^*}, \tag{3.9}$$

where

$$E = \frac{cR_p\rho_e h_{fg}^2}{k_f T_p} \tag{3.10}$$

is the Evaporation number that measures the ratio of the evaporative heat flux at the interface to the conductive heat flux in the liquid, assuming that both are driven by the same temperature difference. For common liquids and pore size R_p>1 μm, E >> 1, as shown in Table 2. At the channel wall, $r_p^*=1$,

$$T^*=1 \tag{3.11}$$

The channel length is taken to be infinity so that as $z_p^* \to \infty$,

$$T^* \to 1 \tag{3.12a}$$

From the solution $T^*=T^*(r_p^*,z_p^*)$, the non-dimensionalized mass evaporation rate at a pore is found as

$$M_p^* = 2\pi \int_0^1 T^*(r_p^*, 0) r_p^* dr_p^* \tag{3.12b}$$

3.3 Asymptotic Solution

The non-dimensionalized liquid temperature is solved in the limit $E \to \infty$. In this limit, the boundary condition at the interface $z_p^* = 0$ becomes $T^* = 0$. Thus, the leading order solution gives zero mass evaporation rate according to (3.12b), and is presented in Appendix B. The leading order solution creates a singularity at the contact line as T^* goes from 1 at the wall to 0 at the interface. This singularity arises because the gradient term in (3.12b) is dropped in the limit $E \to \infty$, suggesting the existence of a boundary layer. To resolve the temperature profile in the boundary layer, the variables are re-scaled to retain the gradient term in the boundary condition:

$$X = E(1 - r_p^*), \qquad Y = E z_p^*, \qquad \tau = T^*(X, Y), \tag{3.13}$$

Where the coordinates (X,Y) originate from the contact line, as shown in Figure 2. The governing equation (3.8) becomes

$$\frac{\partial^2 \tau}{\partial X^2} - \frac{1}{E - X}\frac{\partial \tau}{\partial X} + \frac{\partial^2 \tau}{\partial Y^2} = 0 \tag{3.14}$$

In the limit $E \to \infty$, the governing equation reduces to

$$\frac{\partial^2 \tau}{\partial X^2} + \frac{\partial^2 \tau}{\partial Y^2} = 0 . \tag{3.15}$$

At the interface Y=0,

$$\tau = \frac{\partial \tau}{\partial Y} . \tag{3.16a}$$

At the pore wall X = 0,

$$\tau = 1 . \tag{3.16b}$$

Thus, the system reduces to the two-dimensional Cartesian case solved by Zhang, Watson, and Wong (Zhang, 2007), and the solution is

$$\tau = 1 - \frac{2}{\pi}\tan^{-1}(\frac{X}{Y}) + \frac{2}{\pi}e^{Y}X\int_{Y}^{\infty}\frac{e^{-\lambda}}{\lambda^2 + X^2}d\lambda, \tag{3.17}$$

At the interface Y=0,

$$\tau = \frac{2}{\pi}X\int_{0}^{\infty}\frac{e^{-\lambda}}{\lambda^2 + X^2}d\lambda \tag{3.18}$$

The dimensionless mass evaporation rate per pore is

$$M_p^* = \frac{2\pi}{E}\int_{0}^{E}\tau dX \tag{3.19a}$$

The coordinates are scaled back and τ in (3.18) is substituted in (3.19a) to give

$$M_p^* = 4\int_{0}^{\infty}e^{-\lambda}\int_{0}^{1}\frac{1-r_p^*}{\lambda^2 + E^2(1-r_p^*)^2}dr_p^* d\lambda \tag{3.19b}$$

Solving (3.19b) and ignoring higher order terms,

$$M_p^* = \frac{2}{E}\ln E \tag{3.20}$$

CHAPTER 4. HEAT AND MASS TRANSFER ALONG THE PIPE

The heat pipe is studied under small temperature differences. This makes the flow fields and temperature distribution along the pipe skew-symmetric about the mid-point of the pipe. Thus, only the heated half of the heat pipe is studied.

The vapor pressure p_g varies along the pipe and is related to the local volume flow rate V_g, assuming laminar flow, by

$$\frac{dp_g}{dz} = -\frac{8\mu_g V_g}{\pi R_g^4}, \tag{4.1}$$

where μ_g is the viscosity of the vapor and z is the axial coordinate shown in Figure 1(b). The vapor volume flow rate V_g varies along the pipe owing to evaporation. A local mass balance is performed on a section of the vapor domain, as shown in Figure 3. The section has length $\Delta z = L/N_z$ and includes at the middle N_θ radially pointing capillaries. The rate of vapor mass leaving the section is equal to that entering the section plus the mass evaporated at N_θ pores:

$$\rho_o[V_g(z+\Delta z) - V_g(z)] = N_\theta M_p \tag{4.2a}$$

Applying Taylor's expansion (Struik 1969) and substituting Δz lead to

$$\frac{dV_g}{dz} = \frac{N_\theta N_z M_p}{L\rho_0}, \tag{4.2b}$$

where $M_p = M_p(z)$ is the mass evaporation rate per pore, and ρ_0 is the equilibrium vapor density at T_0. Differentiating (4.1) and substituting V_g from (4.2) gives

$$\frac{d^2 p_g}{dz^2} = -\frac{8\mu_g}{\pi R_g^4}\left[\frac{N_\theta N_z M_p}{L\rho_o}\right] \tag{4.3}$$

This equation shows how the vapor pressure is related to the mass evaporation rate.

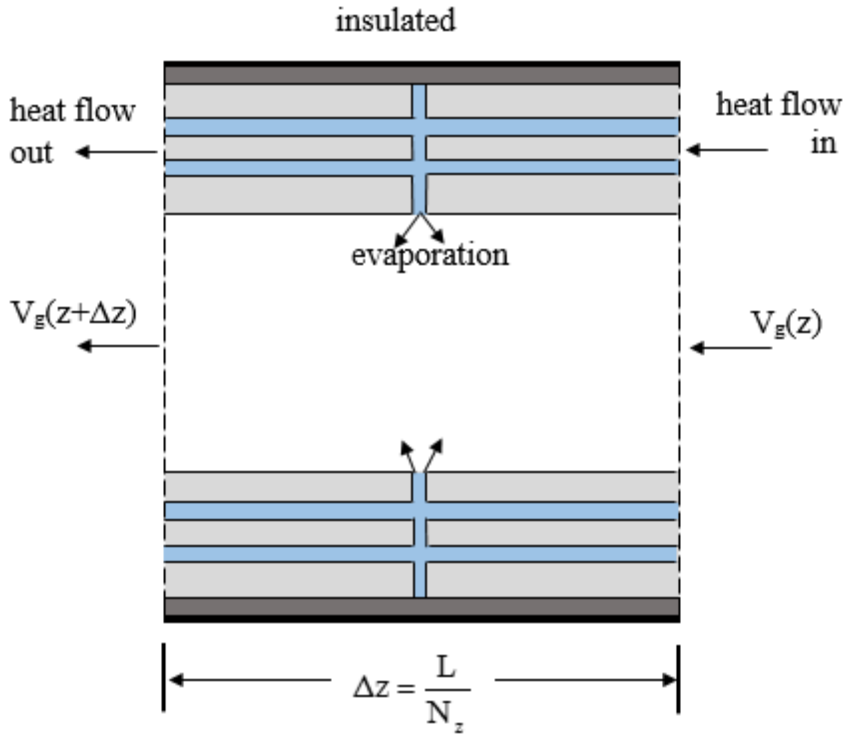

Figure 3. Control volumes for derivation of vapor mass conservation, and thermal energy balance. Both control volumes have length $\Delta z = L/N_z$, which is the length of a unit cell in the axial direction. There are N_θ radial capillaries at the center of thecontrol volumes. The mass conservation control volume encloses only the vapor region, whereas the energy balance control volume excludes the vapor region.

Heat is transferred along the pipe from the hot to the cold end by vapor flow and by conduction in the wick and the pipe wall. Conduction in the vapor is neglected owing to its low thermal conductivity as compared to the liquid, wick and pipe wall materials. We take heat transfer to be one dimensional along the length of the pipe because of the high aspect ratio. Also, at each point along the pipe, the liquid, the wick, and the pipe wall are to be at the same temperature (T_p). The outer wall of the pipe is assumed to be insulated.

An energy balance on a section of the pipe shown in Figure 3 equates the rate of conductive heat energy entering the system to that leaving the system plus the rate of evaporative heat loss:

$$M_p N_\theta h_{fg} = (k_f A_f + k_s A_s + k_w A_w)[\frac{\partial T}{\partial z}(z+\Delta z) - \frac{\partial T}{\partial z}(z)], \tag{4.4a}$$

where k is the thermal conductivity and A is the cross-sectional area with the subscript indicating liquid (f), wick solid (s), or wall (w). Expansion by Taylor's series and substitution of $\Delta z = L/N_z$ gives

$$(k_f A_f + k_s A_s + k_w A_w)\frac{d^2 T_p}{dz^2} - \frac{M_p N_\theta N_z h_{fg}}{L} = 0 \tag{4.4b}$$

The liquid, solid, and wall areas can be calculated using the radii of the capillary, the wick, and the pipe as shown in Figure 1:

$$A_f = N_\theta N_r \pi R_p^2 \tag{4.5a}$$

$$A_s = \pi(R_i^2 - R_g^2 - N_\theta N_r R_p^2) \tag{4.5b}$$

$$A_w = \pi(R_o^2 - R_i^2) \tag{4.5c}$$

The energy balance can be integrated once after M_p in (4.2) has been substituted:

$$-(k_f A_f + k_s A_s + k_w A_w)\frac{dT_p}{dz} + \rho_0 h_{fg} V_g = q, \tag{4.6}$$

where the integration constant q is recognized as the total heat rate along the pipe from the hot towards the cold end and is a constant because the pipe is insulated. It is the sum of the conduction heat rate (first term) and the vapor flow heat rate (second term). This equation shows the heat transfer physics in a cylindrical heat pipe.

There are two dependent variables: T_p and p_g. Each satisfies a second-order ordinary differential equation as shown in (4.3) and (4.4b), because M_p varies linearly with T_p and p_g as explained in the next section. Therefore, the coupled system of equations requires four boundary conditions. At the hot end of the pipe z=0,

$$T_p = T_0 + \Delta T, \tag{4.7}$$

and V_g=0 because there is no vapor flow. Thus, (4.1) gives

$$\frac{dp_g}{dz} = 0 \tag{4.8}$$

At the mid-point of the pipe z=L,

$$T_p = T_o, \tag{4.9}$$

and

$$p_g = P_0. \tag{4.10}$$

Instead of solving the coupled system of equations for p_g and T_p, we find it simpler to solve for the evaporation rate M_p.

CHAPTER 5. EVAPORATION ALONG THE PIPE

The mass evaporation rate M_p at a pore was made dimensionless by (3.7d) into M_p^* and then solved in section 3.3 to yield the solution (3.20). Thus,

$$M_p = c\rho_e h_{fg} 2\pi R_p^2 M_p^*(E) \frac{(T_p - T_g)}{T_p}, \tag{5.1}$$

where T_g is the saturation temperature at pressure p_g, and is expanded about the initial temperature T_0 as

$$T_g = T_0 + \frac{dT_p}{dp_g}(p_g - P_0) + \ldots \tag{5.2}$$

and

$$\frac{dT_g}{dp_g} = \frac{T_0}{\rho_0 h_{fg}} \tag{5.3}$$

by the Clapeyron equation (Bejan 1997). Thus,

$$M_p = c2\pi R_p^2 M_p^*(E)[(T_p - T_0)\frac{\rho_0 h_{fg}}{T_0} - (p_g - P_0)], \tag{5.4}$$

where P_0 is the saturation pressure at T_o,

$$c = \frac{\alpha}{\sqrt{2\pi R_s T_o}}, \tag{5.5}$$

$$E = \frac{cR_p \rho_o h_{fg}^2}{k_f T_o}, \tag{5.6}$$

where only the reference parameters T_o and ρ_o are left in M_p, c, and E because $T_p \approx T_0$. Thus, M_p varies linearly with T_p and p_g.

The mass evaporation rate M_p in (5.4) is differentiated twice to give

$$\frac{d^2M_p}{dz^2} = \frac{2\pi N_\theta N_z R_p^2 c}{L} M^*(E)[\frac{T\rho_0 h_{fg}^2}{T_0(k_f A_f + k_s A_s + k_w A_w)} + \frac{8\mu_g}{\pi R_g^4 \rho_0}]M_p\,, \tag{5.7}$$

where d^2p_g/dz^2 in (4.3) and d^2T_p/dz^2 in (4.4b) have been substituted. Thus, the differential equation for M is decoupled from p_g and T_p.

5.1 Non-dimensionalization

We define a set of dimensionless variables:

$$z^* = \frac{z}{L},\ \ T_p^* = \frac{T_p - T_0}{\Delta T},\ \ p_g^* = \frac{p_g - P_0}{\rho_0 h_{fg}\Delta T/T_0},\ \ M^* = \frac{M_p}{c\rho_0 h_{fg} R_p M_p^*(E)\Delta T/T_0} \tag{5.8 a, b, c, d}$$

The pressure scale $\rho_0 h_{fg}\Delta T/T_0$ = $(dp_e/dT_p)\Delta T$ is the equilibrium vapor pressure difference between the hot end and the mid-point of the pipe. Equation (5.7) becomes

$$\frac{d^2M^*}{dz^{*2}} = S^2 M^*, \tag{5.9}$$

where,

$$S = \{2\pi R_p^2 N_\theta N c M_p^*(E)[\frac{\rho_0 h_{fg}^2}{(k_f A_f + k_s A_s + k_w A_w)T_0} + \frac{8\mu_g}{\pi R_g^4 \rho_0}]\}^{1/2} L\,, \tag{5.10}$$

is the dimensionless exponent that controls the evaporation gradient along the pipe and $N = N_z/L$ is the number density of pores per unit pipe length.

5.2 Boundary Conditions

The boundary conditions for T_p and p_g in Section 4 are converted into boundary conditions for M. Equation (5.4) is made dimensionless as

$$M^* = T_p^* - p_g^*\,. \tag{5.11}$$

At the middle of the pipe $z^*=1$,

$T_p^* = 0$

$p_g^* = 0$

Thus,

$$M^*=0. \tag{5.12}$$

This gives one boundary condition for M^*. At the hot end $z^*=0$,

$$\begin{aligned} T_p^* &= 1, \\ \frac{dp_g^*}{dz^*} &= 0. \end{aligned} \tag{5.12a}$$

To convert these conditions, we need the energy equation (4.6), which after V_g is substituted, becomes

$$\frac{dT_p^*}{dz^*} + H\frac{dp_g^*}{dz^*} = -\frac{q}{q_c}, \tag{5.13}$$

$$H = \frac{\pi\rho_0^2 h_{fg}^2 R_g^4}{8\mu_g T_0 (k_f A_f + k_s A_s + k_w A_w)} \tag{5.14}$$

$$q_c = \frac{(k_f A_f + k_s A_s + k_w A_w)\Delta T}{L} \tag{5.15}$$

where H is the dimensionless heat pipe number that measures the ratio of evaporative heat transfer to conductive heat transfer, and q_c is the conduction heat rate in the pipe in the absence of vapor flow. The above equation is integrated once:

$$T_p^* + Hp_g^* = \frac{q}{q_c}(1 - z^*), \tag{5.16}$$

where the boundary conditions $T_p^* = 0$ and $p_g^* = 0$ at $z^*=1$ have been imposed. At $z^*=0$, $T_p^* = 1$, and p_g^* is eliminated using (5.11) to give

$$M^* = 1 - (\frac{q}{q_c} - 1)\frac{1}{H}. \tag{5.17}$$

Since q is unknown, another boundary condition is needed. Differentiating (5.11) once yields

$$\frac{dM^*}{dz^*} = \frac{dT_p^*}{dz^*} - \frac{dp_g^*}{dz^*}. \tag{5.18}$$

At $z^*=0$, $dp_g^* / dz^* = 0$ and the above equation together with (5.13) gives

$$\frac{dM^*}{dz^*} = \frac{dT_p^*}{dz^*} = -\frac{q}{q_c}. \tag{5.19}$$

Thus, q/q_c is substituted into (5.17) to give

$$\frac{dM^*}{dz^*} = (M^* - 1)H - 1. \tag{5.20}$$

This is the second boundary condition for M^*.

5.3 Solution

Second order non-dimensional mass evaporation rate is solved using the boundary conditions to give

$$M^* = \frac{(1+H)\sinh[S(1-z^*)]}{(S + H\tanh S)\cosh S} \tag{5.21}$$

The solution is plotted in figure 4 and figure 5 for S=1 and S=100 respectively. When S=1, evaporation occurs almost linearly along the heated half of the pipe because in the limit $S \to 0$, $M^* \to (1 - z^*) + \ldots$. When S=100, all the evaporation occurs in a boundary layer near the hot end. This follows from the solution in the limit $S \to \infty$,

$$M^* \to \frac{(1+H)}{(S+H)} e^{-Sz^*} + \ldots. \tag{5.22}$$

At $z^*=0$, $M^* \to (1+H)/S$ if H<<S and $M^* \to 1$ if H>>S.

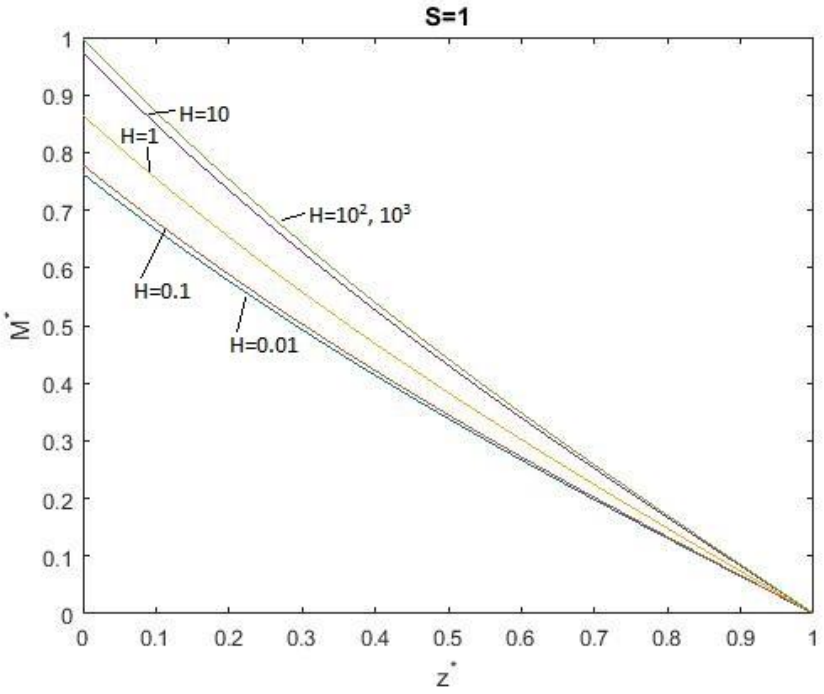

Figure 4. Dimensionless evaporation rate along the pipe for various H and S=1

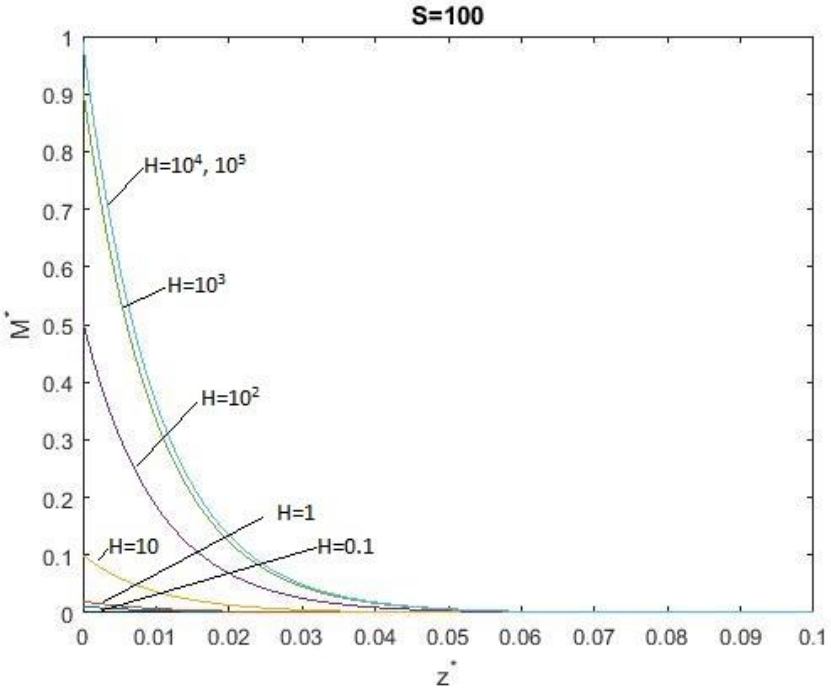

Figure 5. Dimensionless evaporation rate along the pipe for various H and S=100

CHAPTER 6. NUSSELT NUMBER

The Nusselt number Nu, defined as the ratio of the total heat rate to the conduction heat rate, is obtained from (4.15) after substituting the solution for M^* in (4.18):

$$Nu = \frac{q}{q_c} = \frac{1+H}{1+H(\tanh S)/S} \tag{6.1}$$

The solution is plotted in figure 6.

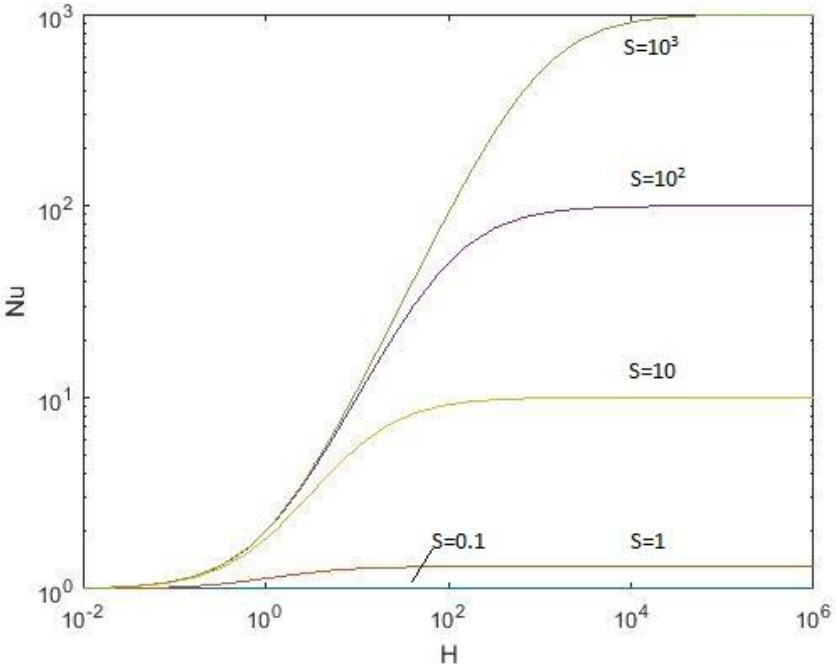

Figure 6. Nusselt Number versus H for various S

CHAPTER 7. PIPE TEMPERATURE

The vapor pressure p_g^* is eliminated from (5.11) and (5.19) to give the pipe temperature T_p^*:

$$T_p^* = \frac{S}{S + H \tanh S}\{(1 - z^*) + \frac{H \sinh[S(1 - z^*)]}{S \cosh S}\} \tag{7.1}$$

The solution is plotted in figure 7 and figure 8 for S=1 and 100 respectively. When S=1, conduction heat transfer dominates and an almost linear temperature profile is obtained for all values of H.

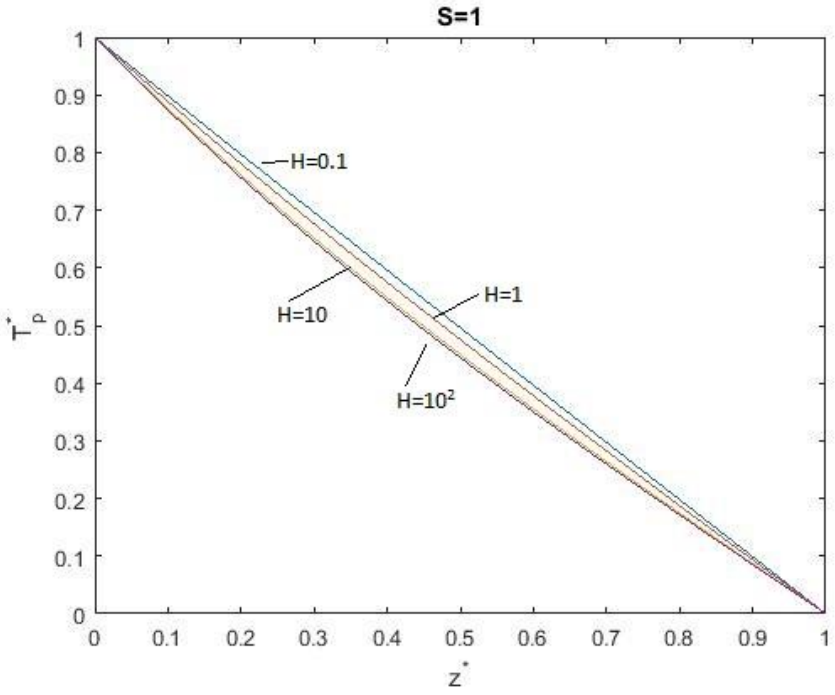

Figure 7. Dimensionless temperature along the pipe for various H and S=1

This is because in the limit $S \to 0$, Eqn 7.1 gives $T^*_p \to (1\text{-}z^*)+\ldots$, independent of H. The pipe temperature for S=100 is plotted in Figure 8.

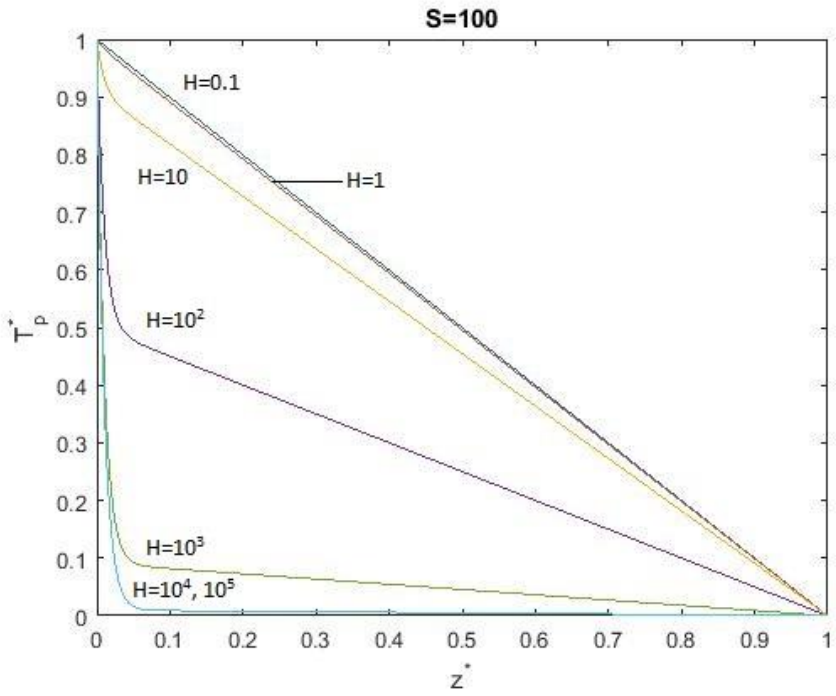

Figure 8. Dimensionless temperature along the pipe for various H and S=100

When H=0.1, there is little heat transfer by vapor flow, and conduction dominates, resulting in a linear temperature profile. At high H, vapor-flow heat transfer dominates and removes a large amount of thermal energy from the hot end. This decreases the temperature rapidly in a boundary layer near the hot end. Outside the boundary layer there is little evaporation and heat is transferred mainly by conduction, resulting in a linear temperature profile. This is shown by the solution in the limit, $S \to \infty$

$$T_p^* \to \frac{S}{S+H}[(1-z^*)+\frac{H}{S}e^{-Sz^*}]+... \tag{7.2}$$

For H<<S,

$$T_p^* \to 1-z^*+O(H/S). \tag{7.3}$$

For H>>S,

$$T_p^* \to e^{-Sz^*}+\frac{S}{H}(1-z^*)+... \tag{7.4}$$

This shows a thermal boundary layer near $z^*=0$, and a linear profile away from the boundary layer. The thickness of the boundary layer is scaled by S^{-1}. The boundary layer is the evaporating region of the heat pipe. Outside the boundary layer, $T^*_p = O(S/H) << 1$ along the pipe. This is the adiabatic region. Since the temperature profile is skew-symmetric about the mid-point of the pipe, a similar boundary layer exists at the cold end (the condensing region).

CHAPTER 8. VAPOR PRESSURE AND VOLUME FLOW RATE ALONG THE PIPE

Substituting M^* in (5.22) and T^*_p in (7.1) into (5.11) gives the vapor pressure p^*_g as

$$p_g^* = \frac{S}{S + H\tanh S}\{(1 - z^*) - \frac{\sinh[S(1 - z^*)]}{S\cosh S}\}. \tag{8.1}$$

The solution is plotted in Figure 9 and 10 for S=1 and S=100, respectively. They show that the pressure gradient decreases as H increases for a constant S.

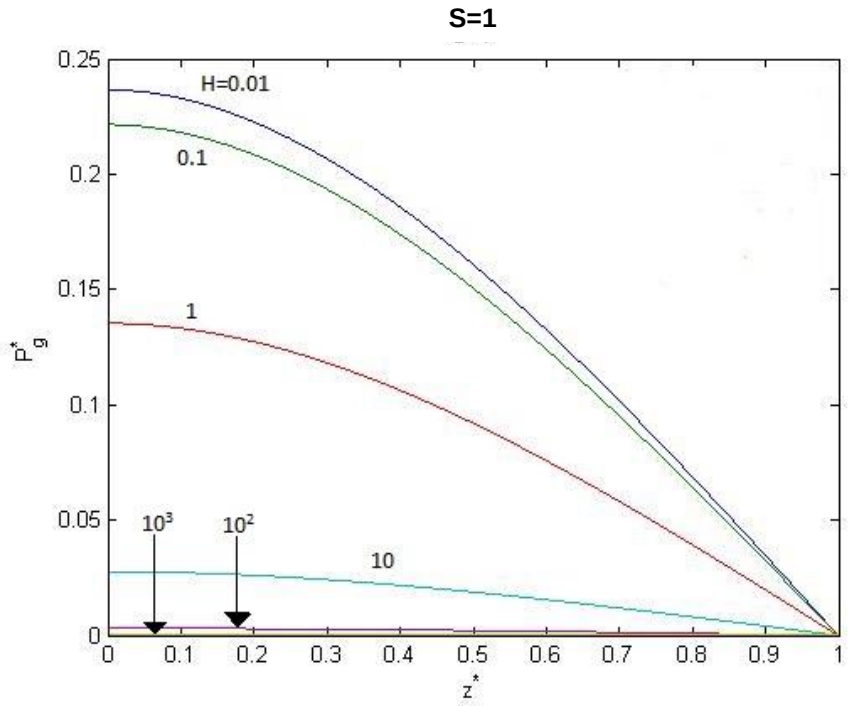

Figure 9. Dimensionless vapor pressure along the pipe for various H and S=1

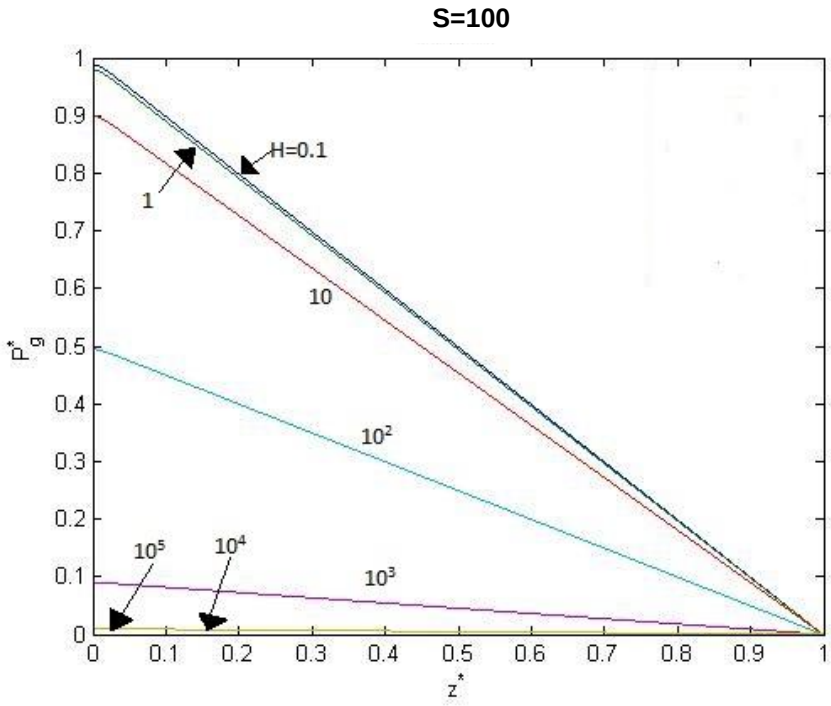

Figure 10. Dimensionless vapor pressure along the pipe for various H and S=100

The vapor volume flow rate V_g is made dimensionless using the scale $\delta V_g = cR_i M^*(E)(dp_e/dT_p)\Delta TL/\rho_0$ obtained from (3.2): $V_g^* = V_g/\delta V_g$. Thus (3.2) becomes:

$$\frac{dV_g^*}{dz^*} = M^* \tag{8.2}$$

This equation is integrated once subject to the boundary condition $V^*_g = 0$ at $z^* = 0$:

$$V_g^* = \frac{(1+H)}{S(S+H\tanh S)}\{1-\frac{\cosh[S(1-z^*)]}{\cosh S}\} \tag{8.3}$$

The solution is plotted in Figure 11 and 12 for S=1 and 100, respectively. As $S \to 0$, 8.3 gives

$$V_g^* \to z^*(1-\frac{z^*}{2})+... \tag{8.4}$$

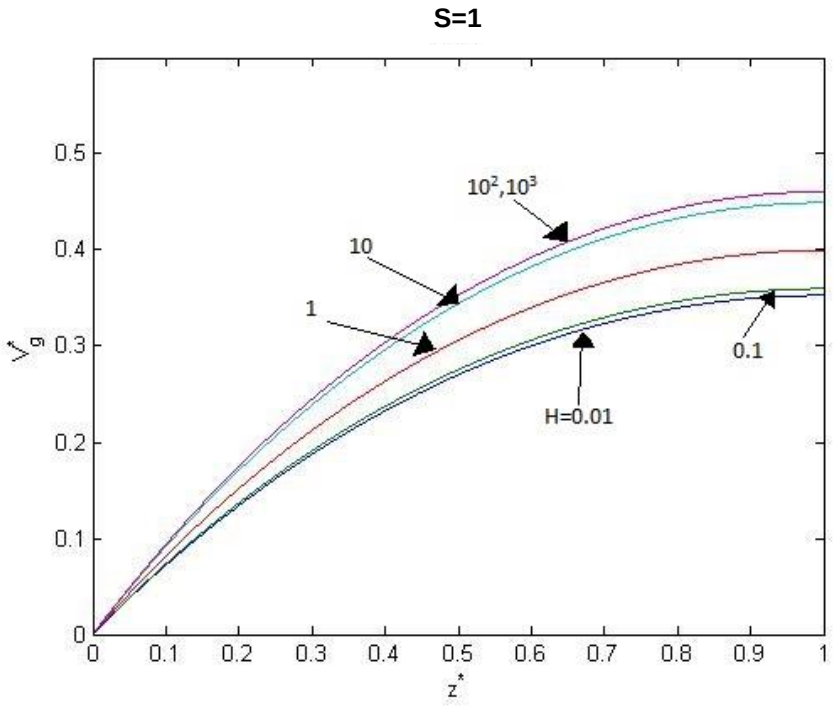

Figure 11. Dimensionless vapor volume flow rate along the pipe for various H and S=1

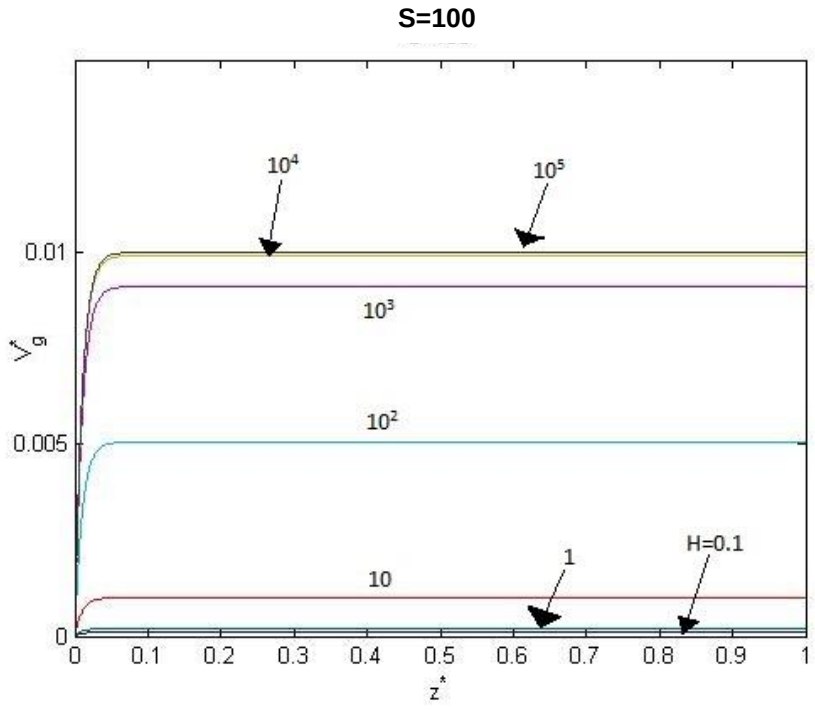

Figure 12. Dimensionless vapor volume flow rate along the pipe for various H and S=100

This explains the parabolic growth in Figure 11. As $S \to \infty$,

$$V_g^* = \frac{(1+H)}{S(S+H)}(1-e^{-Sz^*}) + \ldots \tag{8.5}$$

Thus, V^*_g increases from 0 to a constant level within the thermal boundary layer. The constant level approaches $(1+H)/S^2$ for H<<S, and 1/S for H>>S. These asymptotic results explain the behavior of V^*_g in Figure 14.

The vapor volume flow rate V^*_g is closely related to the vapor pressure p^*_g. When V^*_g is constant along the pipe in Fig. 12, the pressure gradient is constant as shown in Fig. 10. When V^*_g is increasing along the pipe in Figure 14, the pressure gradient must also increase (Fig. 9). Although V^*_g increases with H for a given S, p^*_g decreases with H. This is because p^*_g is made dimensionless by the equilibrium vapor pressure drop $\Delta T(dp_e/dT_p)$. As V^*_g increases, the equilibrium vapor pressure drop cannot be sustained, and Δp_g across the pipe must decrease compared with $\Delta T(dp_e/dT_p)$.

Equation 4.1 is made dimensionless to yield

$$\frac{dp_g^*}{dz^*} = -RV_g^* \tag{8.6}$$

Here,

$$R = \frac{S^2}{(1+H)} \tag{8.7}$$

represents the dimensionless viscous resistance to vapor flow. As $S \to 0$, V^*_g becomes independent of S and H to leading order, as shown in 8.4. Thus, $\left|dp_g^*/dz^*\right|$ for fixed S(<<1)

decreases as H increases as shown in Fig. 11. As $S \to \infty$, V^*_g is constant along most part of the pipe (Fig. 14). For H<<S, the constant level approaches (1+H)/S^2, so that, $dp^*_g / dz^* \to -1$ as observed in Fig. 10 for H=0.1 and 1. For H>>S, the constant level approaches 1/S, so that $dp^*_g / dz^* \to -S/H$, as seen in Figure 10 for H=10^3 and 10^4.

CHAPTER 9. LIQUID FLOW ALONG THE PIPE

Since the heat pipe is a close system, the vapor mass flow rate at each point along the pipe must be equal to and opposite of the liquid mass flow rate:

$$V_g \rho_g = -V_f \rho_f \tag{9.1}$$

The negative sign is needed because both V_g and V_f are defined positive in the z direction (Figure 1(b)). The liquid flow is assumed to divide evenly among the $N_r N_\theta$ circular channels along the pipe. Since the channels are small, the liquid flow is laminar and the liquid pressure gradient varies linearly with the volume flow rate:

$$\frac{dp_f}{dz} = \rho_f g_z - \frac{8\mu_f}{\pi R_p^4}\left[\frac{V_f}{N_r N_\theta}\right] \tag{9.2}$$

Where, g_z is the acceleration due to gravity along the z-direction. Since V_f varies linearly with V_g, which in turn varies linearly with the vapor pressure gradient as shown in (4.1),

$$\frac{dp_f}{dz} = \rho_f g_z - \frac{1}{N_r N_\theta}\frac{\rho_g \mu_f}{\rho_f \mu_g}\left(\frac{R_g}{R_p}\right)^4 \frac{dp_g}{dz} \tag{9.3}$$

At the mid-point of the pipe z=L, the vapor pressure is equal to the liquid pressure

$$p_f = p_g = P_o \tag{9.4}$$

Integrating (9.2) and applying the condition (9.4), the liquid pressure can be calculated as

$$p_f = \rho_f g_z (z - L) + \frac{1}{N_r N_\theta}\frac{\rho_g \mu_f}{\rho_f \mu_g}\left(\frac{R_g}{R_p}\right)^4 [P_o - p_g] + P_o \tag{9.5}$$

Thus, the liquid pressure varies linearly with vapor pressure along the pipe.

CHAPTER 10. INTERFACIAL CURVATURE VARIATION ALONG THE PIPE

The interfacial curvature at a pore can be determined using the Young-Laplace equation (Wong 1992) as:

$$p_g - p_f = \sigma\kappa \tag{10.1}$$

Here, κ is the curvature and σ is the surface tension (Wong 1992). Therefore, the curvature can be found in terms of the vapor pressure as

$$\kappa = \frac{\rho_f g_z (L-z)}{\sigma} + \frac{(p_g - P_0)}{\sigma}\left[\frac{1}{N_r N_\theta}\frac{\rho_g \mu_f}{\rho_f \mu_g}\left(\frac{R_g}{R_p}\right)^4 + 1\right] \tag{10.2}$$

The curvature depends on the vapor pressure and there is no curvature at the middle of the pipe since z=L and p_g=P_o.

The curvature can provide an estimate for the dry-out temperature difference ΔT_D. The radius of the curvature (r_c) of the liquid-vapor interface is related to the curvature by

$$\kappa = \frac{2}{r_c} \tag{10.3}$$

Dry out starts in the pore when the radius of the curvature of the interface is equal to the radius of the pore (r_c=R_p). Hence, using this condition, the imposed temperature difference ΔT_D at which there will be dry-out can be calculated. The non-dimensional form of p_g in (5.8c) is substituted into (10.2) to give

$$\frac{\rho_f g_z (L-z)}{\sigma} + \frac{(\rho_0 h_{fg} \Delta T_D p_g^*)}{T_0 \sigma}\left[\frac{1}{N_r N_\theta}\frac{\rho_g \mu_f}{\rho_f \mu_g}\left(\frac{R_g}{R_p}\right)^4 + 1\right] = \frac{2}{R_p} \tag{10.4}$$

Here ΔT_D is used in place of ΔT since r_c is assumed to be equal to R_p. Next, p_g^* in (8.1) is substituted. During this substitution, z^* is set to zero as dry-out starts first at the end of the pipe. Substituting p_g^* and rearranging terms will give

$$\frac{\Delta T_D}{T_0} = \frac{2(\frac{\sigma}{\rho_0 h_{fg} R_p})(1-\frac{\rho_f g_z L R_p}{\sigma})(\frac{S+H\tanh S}{S-\tanh S})}{\frac{1}{N_r N_\theta}\frac{\rho_g \mu_f}{\rho_f \mu_g}(\frac{R_g}{R_p})^4+1} \tag{10.5}$$

This is the normalized temperature difference that will induce dry out at the hot end. For our model to be valid, we need $\Delta T << \Delta T_D$.

CHAPTER 11. OPTIMUM PIPE LENGTH

The evaporative heat rate should peak at a particular pipe length for a given pipe cross-sectional shape and size, working fluid, and operating temperature. Therefore, finding this optimal pipe length for evaporative heat transfer will help design the most efficient heat pipe (Rao 2015).

The evaporative heat rate is

$$q_v = q - q_c = (Nu - 1)q_c \tag{11.1}$$

Both Nu and q_c depend on pipe length L; Nu=Nu(H,S) according to (6.1), where H defined in (5.14) is independent of L, and S defined in (5.10) can be written as $S = L/\delta z$ in which

$$\delta z = \{N_\theta N_{dz} R_p c M^*(E)[\frac{\rho_0 h_{fg}^2}{(A_w k_w + A_s k_s + A_f k_f)T_0} + \frac{8\mu_g}{\pi R_g^4 \rho_0}]\}^{-1/2} \tag{11.2}$$

is a dimensional length scale independent of L. The conductive heat rate q_c is defined in (5.9) and depends on L. However, we define $\hat{q}_c$ as:

$$\hat{q}_c = \frac{(A_w k_w + A_s k_s + A_f k_f)\Delta T}{\delta z} \tag{11.3}$$

which is independent of L and is used to make q_v dimensionless:

$$q_v^* = \frac{q_v}{\hat{q}_c} = \frac{H(S - \tanh S)}{S(S + H \tanh S)}, \tag{11.4}$$

where $S = L/\delta z$ can be viewed as L made dimensionless by δz. q^*_v is plotted as a function of S for various H. It shows that q^*_v peaks at $S=S_m$ that depends on H. The point S_m is found to obey

$$(S_m - \tanh S_m)^2 - (1 + H))\tanh^2 S_m - S_m^2 \operatorname{sech}^2 S_m) = 0 \tag{11.5}$$

This equation can be solved numerically using bisection method (Kaw 2003). In the limit of $S_m \to \infty$, (11.5) is expanded and solved to give

$$S_m \to 1+(1+H)^{1/2}+\ldots \tag{11.6}$$

Figure (13) shows that the numerical and asymptotic solutions agree with each other.

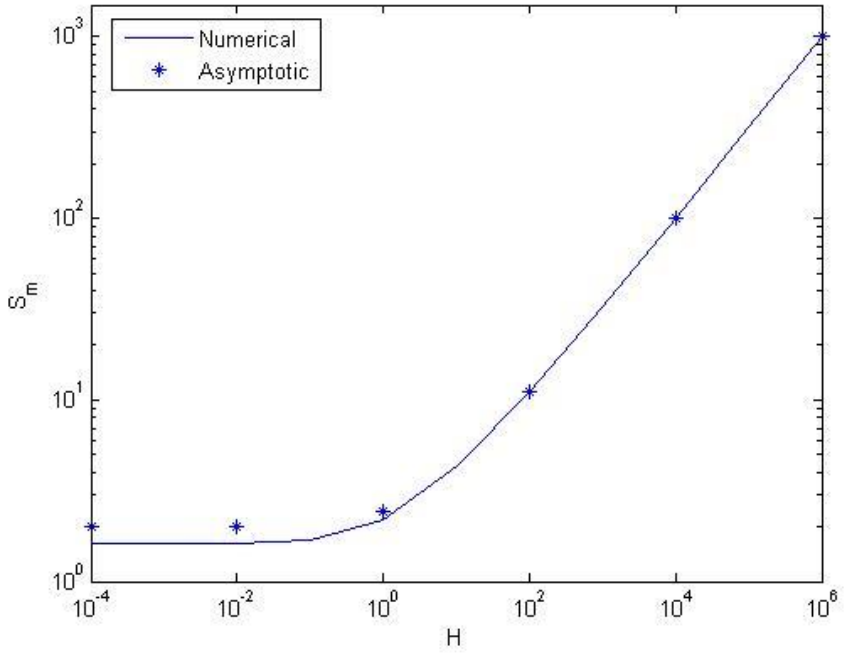

Figure 13. Optimum pipe length S_m versus H

The physical significance of the dimensionless optimum pipe length S_m can be understood through Fig 14. It shows that the normalized evaporative heat rate q^*_v approaches zero as $S \to 0$ and $S \to \infty$. For short pipes ($S \to 0$), conduction dominates because $Nu \to 1$ as $S \to 0$. Thus, $q_v^* \to 0$. For long pipes ($S \to \infty$), the evaporation rate $M^* \to 0$ in (5.22), and thus $q_v^* \to 0$.

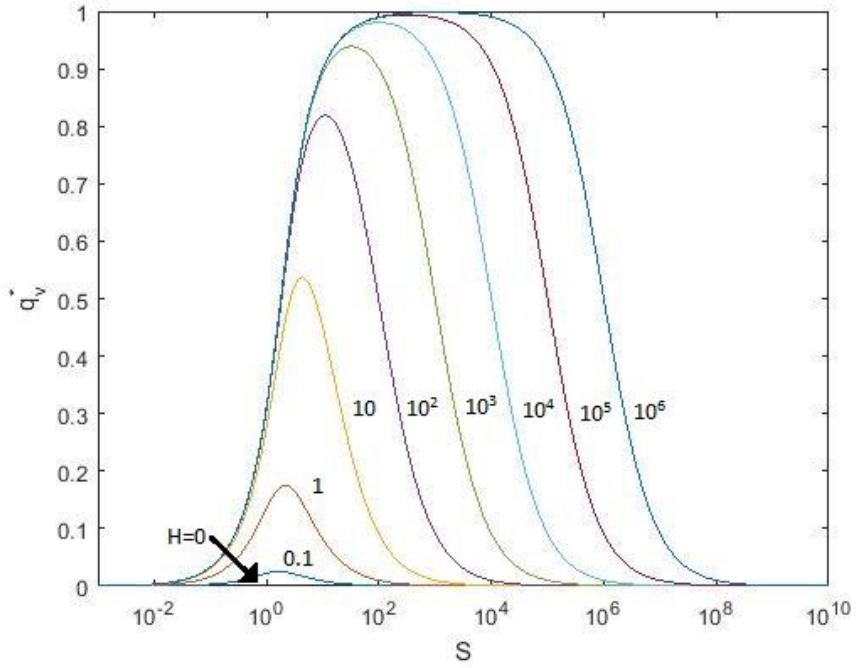

Figure 14. Dimensionless vapor flow heat rate versus S for various H

CHAPTER 12. OPTIMUM WICK THICKNESS

For fixed pipe length and ΔT, there should be an optimum wick thickness for maximum evaporative heat transfer. To find the optimum wick thickness, we define the ratio of wick radius to the inner wall radius, $R_g^*=R_g/R_i$. Hence, the optimization starts by non-dimensionalizing the evaporative heat rate q_v in equation (11.1). However, the heat-rate scales q_c and $\hat{q}_c$ depend on R_g. Therefore, we define a new scale:

$$q_w = k_w A_w \frac{\Delta T}{L}, \tag{12.1}$$

which is not affected by the wick radius. Therefore,

$$\bar{q}_v = \frac{q_v}{q_w} = (Nu - 1)\frac{k_f A_f + k_s A_s + k_w A_w}{k_w A_w}. \tag{12.2}$$

This non-dimensional evaporation heat rate can be plotted against the radius ratio R_g^* to get the optimum radius. Equation (12.2) is expanded to show the relation between $\bar{q}_v$ and R_g^*:

$$\bar{q}_v = \left(\frac{1+H}{1+H(\tanh S)/S} - 1\right)\frac{k_f^* N^{*2}(1-R_g^{*2}) + k_s^*(1-R_g^{*2})(1-N^{*2}\pi) + (R_0^{*2}-1)}{(R_0^{*2}-1)} \tag{12.3}$$

Here, $R_o^*=R_o/R_i$, $k_f^*=k_f/k_w$, $k_s^*=k_s/k_w$, and $N^*=NR_p$. Similarly, H and S can also be written in terms of R_g^* and other dimensionless terms as

$$H = \frac{1}{8}\frac{H_w R_g^{*4}}{k_f^* N^{*2}(1-R_g^{*2}) + k_s^*(1-R_g^{*2})(1-\pi N^{*2}) + (R_o^{*2}-1)} \tag{12.4a}$$

$$S = \{16\pi N^{*2}\frac{(1+R_g^*)}{R_g^{*4}} M_p^*(E)\frac{1}{\mathrm{Re}_c}[H+1]\}^{1/2} L^* \tag{12.4b}$$

Here, $L^*=L/R_i$, $H_w = \dfrac{\rho_0^2 h_{fg}^2 R_i^2}{\mu_g T_0 k_w}$, and $\mathrm{Re} = \dfrac{\rho_0 R_i}{\mu_g c}$. Therefore, $\bar{q}_v$ is shown to depend on R_g^*, once the dimensionless groups in (12.3) and (12.5) have been specified. In Figures 15, 16 and 17 H, S, and $\bar{q}_v$ are plotted as a function of R_g^* for different H_w and for $R_o^*=1.2$, $k_f^*=0.1$, $k_s^*=1$, $N^*=0.1$, $L^*=20$, $\mathrm{Re}=10^4$, $M_p^*(E)=0.01$. It shows that $\bar{q}_v$ reaches a maximum at a particular value of R_g^*.

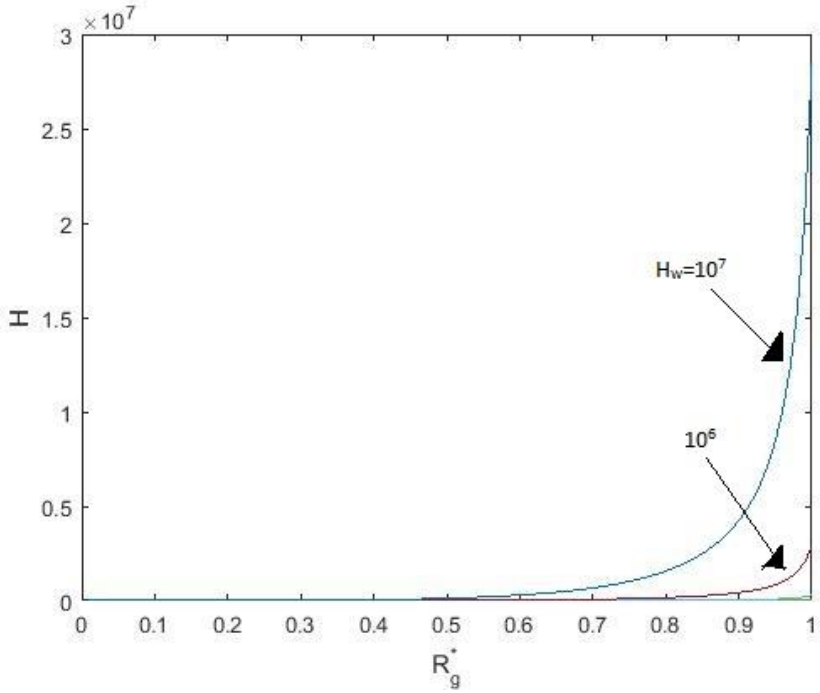

Figure 15. Heat Pipe number versus R_g^* for various H_w

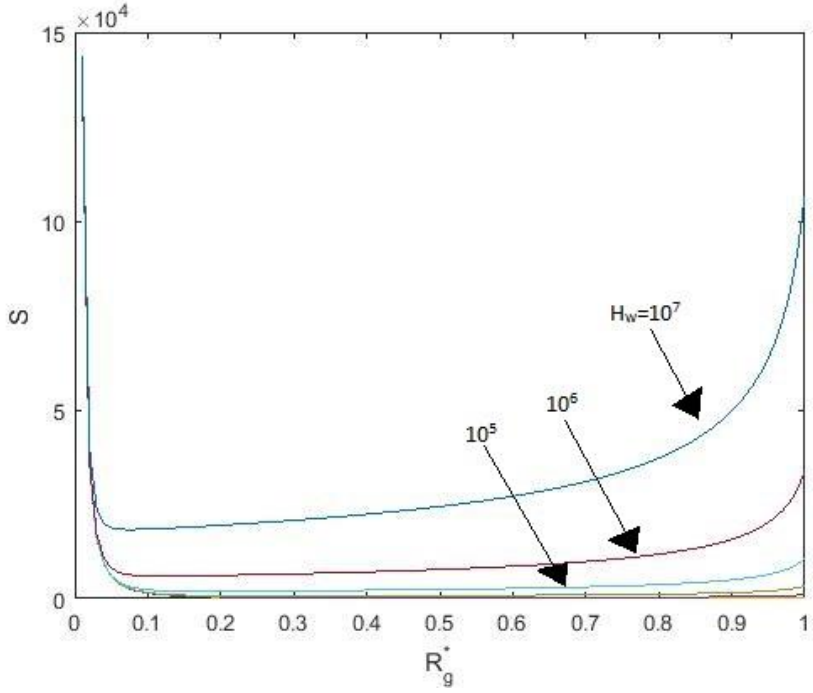

Figure 16. Evaporation Exponent versus R_g^* for various H_w

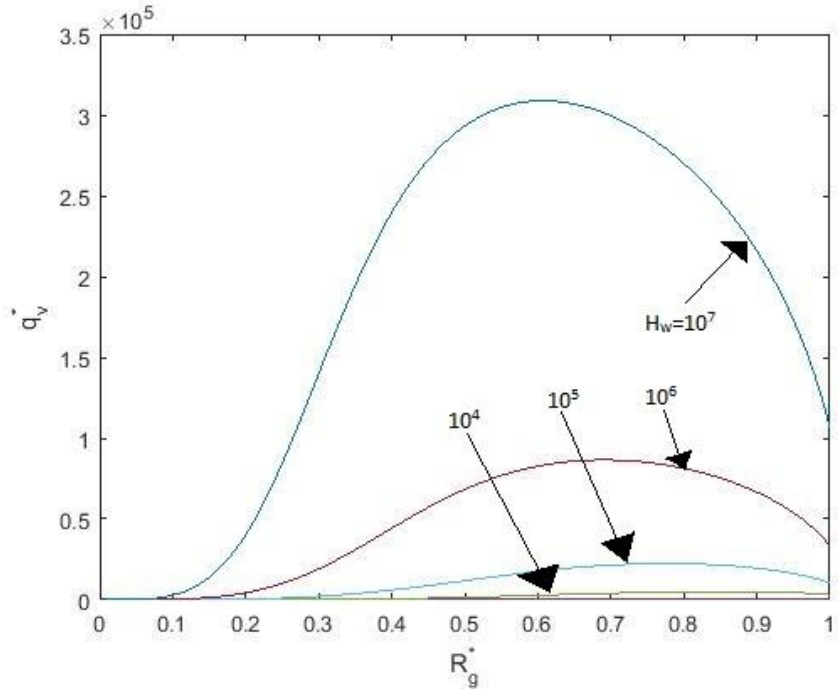

Figure 17. Dimensionless vapor flow heat rate versus R_g^* for various H_w

Similarly, Figures 18, and 19 shows S and $\bar{q}_v$ plotted against R_g^* for various L^*, with others parameters same as before and $H_w=10^7$. H does not change with L^*, so it will be the same as Figure 15 for $H_w=10^7$ case.

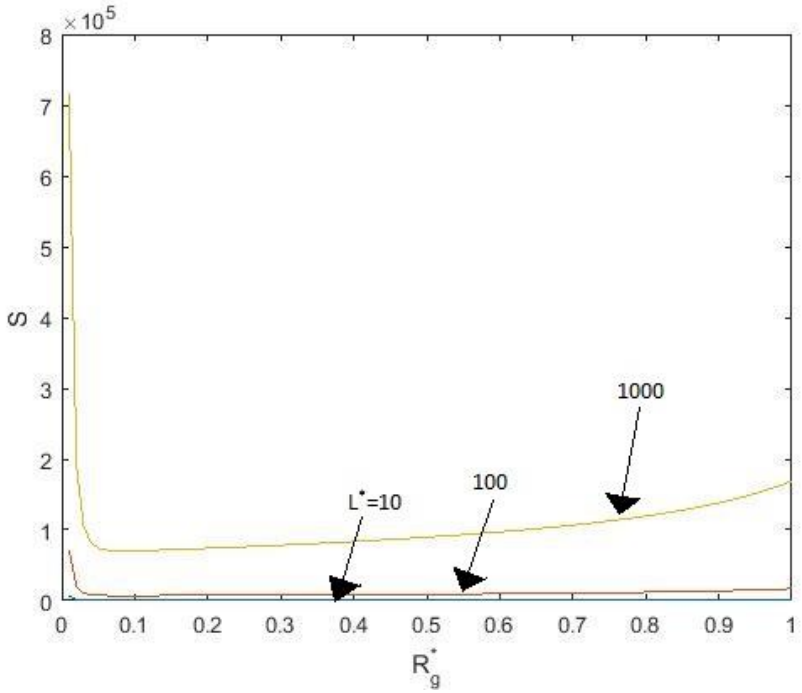

Figure 18. Evaporation Exponent versus R_g^* for various L^*

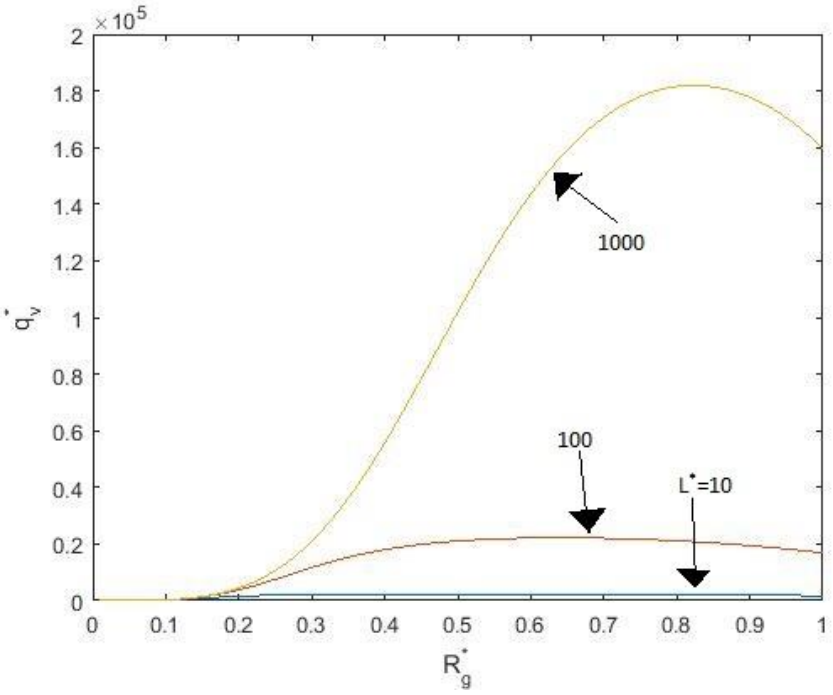

Figure 19. Dimensionless vapor flow heat rate versus R_g^* for various L^*

Finally, in Figures 20, 21, and 22 H, S and $\bar{q}_v$ are plotted against R_g^* for various N^*, fixing other parameters to the values same as above. The variation in the value of H with N^* is very small and cannot be observed in Figure 20.

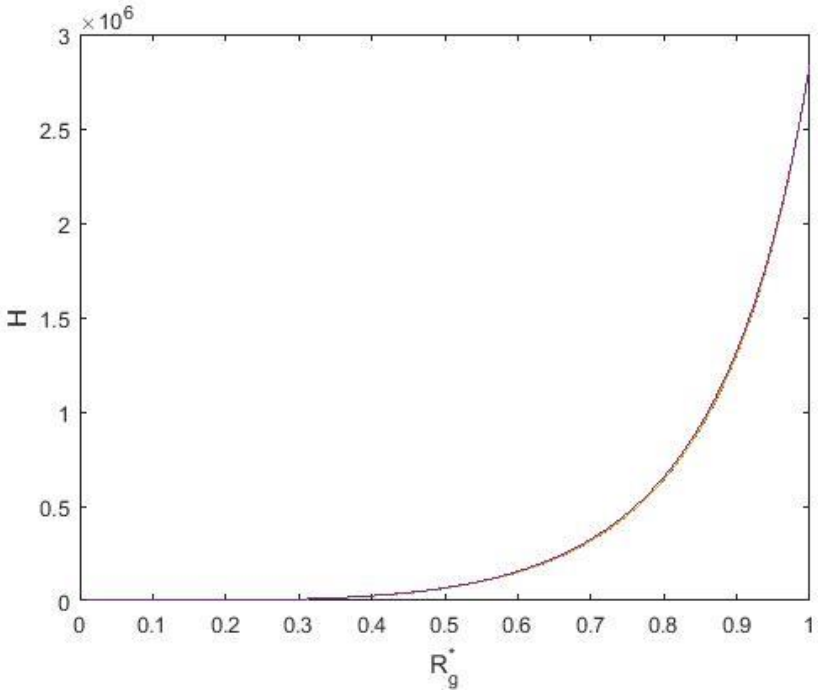

Figure 20. Heat Pipe number versus R_g^* for various N^*

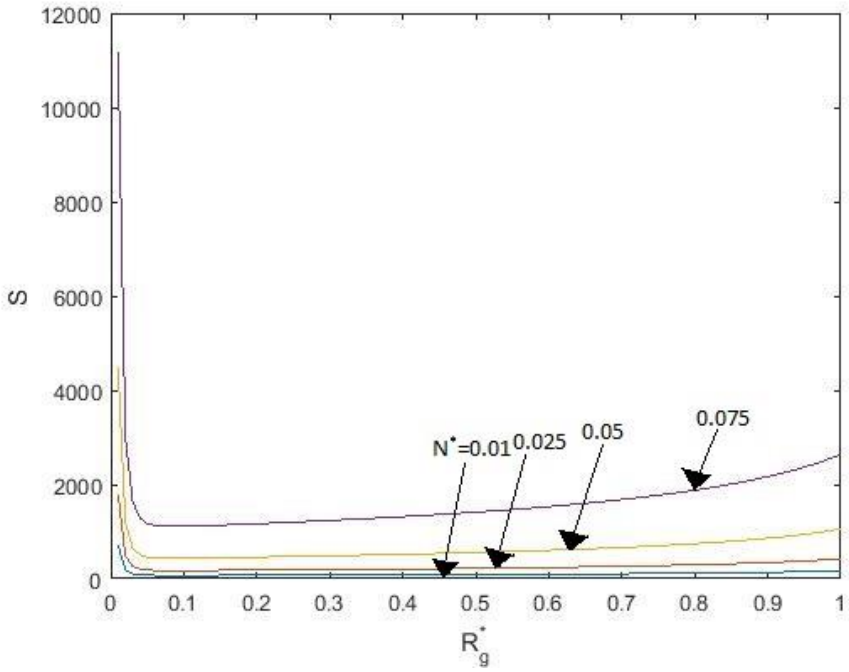

Figure 21. Evaporation Exponent versus R_g^* for various N^*

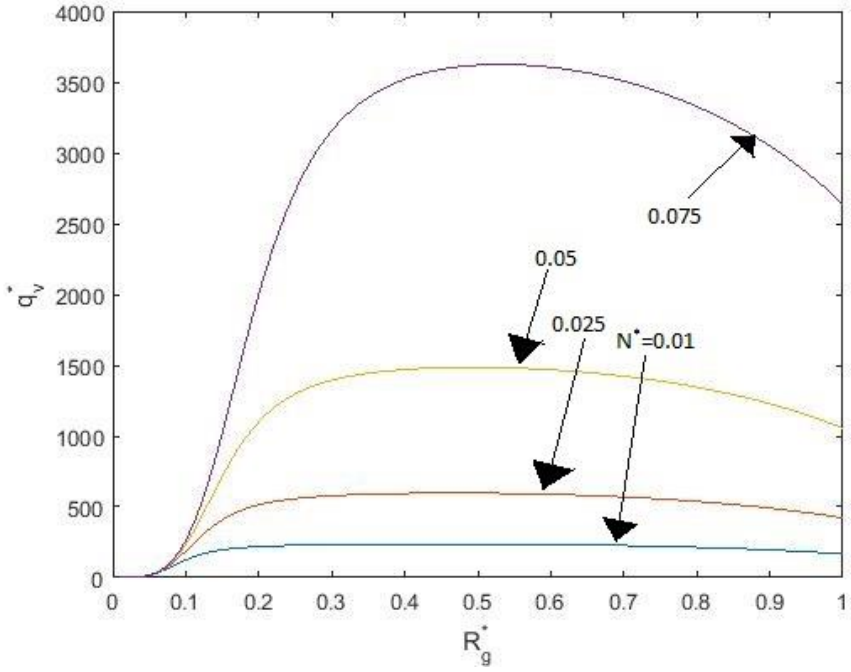

Figure 22. Dimensionless vapor flow heat rate versus R_g^* for various N^*

‘

CHAPTER 13. APPLICATION TO A POROUS MEDIUM

The wick of the modeled heat pipe contains liquid-filled circular capillaries in the axial and radial directions. This idealized wick structure allows an analytic solution for the evaporation rate at a pore which leads to analytic solution for fluid flow and heat transfer. However, common heat pipes use porous media as the wick. A porous medium is characterized by the porosity φ and permeability K. Here, we show a way to relate the modeled wick parameters (N_r, N_θ, N_z, and R_p) to φ and K.

According to Darcy's law (Whitaker, 1986), the volume flow rate Q through a porous media is related to the pressure gradient dp/dz by

$$Q = -\frac{KA}{\mu}\frac{dp}{dz} \tag{13.1}$$

where A is the cross-sectional area of the medium, μ is the fluid viscosity, K is the permeability, and z points in the flow direction.

In our modeled wick, the liquid volume flow rate Q_s in a single circular capillary is related to the pressure gradient by

$$Q_s = \frac{\pi R_p^{\ 4}}{8\mu}(-\frac{dp}{dx}) \tag{13.2}$$

For the entire heat pipe, the total liquid volume flow rate is

$$Q = N_r N_\theta Q_s = -\frac{\pi N_r N_\theta R_p^{\ 4}}{8\mu}(\frac{dp}{dz}) \tag{13.3}$$

By comparing (12.1) and (12.3), we find

$$\mathrm{K} = \frac{N_r N_\theta R_p^4}{8(R_i^2 - R_g^2)}, \tag{13.4}$$

where we have substituted A= π (R_o^2 – R_i^2) for the modeled wick. Further, porosity is defined as the ratio of volume of the pores to the total volume of the wick. The total pore volume consists of the axial and radial capillaries, so that

$$\varphi = \frac{N_r N_\theta \pi R_p^2 L + N_z N_\theta \pi R_p^2 (R_i - R_g)}{\pi (R_i^2 - R_g^2) L} \tag{13.5}$$

For a porous medium, the number of pores per unit length in the axial direction should be the same as that in the circumferential direction and in the radial direction:

$$\frac{N_z}{L} = \frac{N_\theta}{\pi (R_i + R_g)} = \frac{N_r}{R_i - R_g} = N \,, \tag{13.6}$$

where N is the number density. Thus, (12.4) and (12.5) can be written as

$$K = \frac{\pi}{8} R_p^2 N^2 , \tag{13.7}$$

$$\varphi = 2\pi R_p^2 N^2 . \tag{13.8}$$

From these equations, we find

$$R_p^2 = \frac{16K}{\varphi} , \tag{13.9a}$$

and

$$N^2 = \frac{\varphi^2}{32\pi K} . \tag{13.9b}$$

Thus, once φ and K are specified, we can find R_p and N, and (12.6) then yields N_r, N_θ, and N_z.

CHAPTER 14. COMPARISON WITH EXPERIMENTS

Several experiments have been conducted to study the behavior of heat pipes. Kemme investigated a sodium heat pipe to test the limitations imposed by sonic vapor flow (Kemme 1969). The dimensions used are shown in Table 1. Stainless steel wall and mesh were used to construct the heat pipe. The mesh was compressed using copper tube which was later dissolved away. Enough liquid was added to fill the annulus and to saturate the porous tube. Similarly, Tournier and El-Genk analyzed two dimensional water heat pipe with copper as the porous material and the wall (Tournier 1993).

In experiment K, the average radius of the pore, length of the evaporator and the condenser region, inner and outer radius of the pipe, the thickness of the porous material and the mesh size of the screen is given. From the mesh size, N_z. From (13.6), N_θ and N_z are calculated. The length of the entire heat pipe is taken and L is used as the half length of the pipe. Similarly, for experiment TE, the porosity, permeability, the radius of the pore, inner and outer radius of the pipe wall, the thickness of the porous material, and the length of the evaporator section, adiabatic section and the condenser section are provided. Using equations (13.6) and (13.9b), the values for N_θ and N_z are calculated. For both the experiments, the fluid properties like viscosity (μ), density (ρ), latent heat of vaporization (h_{fg}) and thermal conductivity (k) are based on the material. The density and thermal conductivity is taken at the initial temperature T_0. The thermal conductivities were taken from the reference data by Ramires (Ramires 1995). The densities of water were taken from the handbook by Speight (Speight 2005). The densities of sodium were taken from the work by Fink (Fink 1995). Using these fluid properties, dimensions and the imposed conditions on the heat pipe, the evaporation number (E), evaporation exponent (S) and the heat pipe number (H)

were calculated Finally, Nusselt number was calculated using equation (6.1) and compared with the experimental Nusselt number calculated from power in the experiments. All of these values are presented in Table 1.

PARAMETER	K	TE
R_o (x 10^{-2} m)	1.38	1.91
R_i (x 10^{-2} m)	1.20	1.79
R_g (x 10^{-2} m)	1.18	1.66
L (x 10^{-2} m)	1.28	44.5
R_p (x 10^{-6} m)	9.5	54
N_r	8	4
N_θ	360	675
N_z	6089	209
ρ_o (kg/m^3)	0.294	0.396
ρ_f (kg/m^3)	968	966
μ (x 10^{-4} Pa.s)	2.27	0.119
h_{fg} (x 10^3 J/kg)	4240	2250
k_w (W/mK)	45	400
k_s (W/mK)	45	400
k_f (W/mK)	60	0.58
T_o (K)	823	296.2
α	1	0.1
c (x 10^{-4} s/m)	6.47	1.08
E	2166	858

S	21856	1354
H (x 10^6)	8.8	79.8
NU (experiment)	28149	1088
NU (Eqn 6.1)	21856	1354

Table 1. Properties of Heat Pipe used in experiment K by Kemme and TE by Tournier and El-Genk

In experiment K, the Nusselt number was within 22 % of the theoretical value. Similarly, in experiment TE, it was within 20 %.

CHAPTER 15. DISCUSSION

It is interesting that the two-dimensionless parameter H and S are independent of surface tension. This is because the capillary pressure, which depends on surface tension, plays a passive role in cylindrical heat pipes. It serves only to satisfy a mass balance by transporting liquid from the cold end to the hot end. Furthermore, the two dimensionless numbers are independent of the temperature difference between the two ends of the pipe. Thus, driving the pipe at larger temperature difference will not increase Nu.

In addition, by calculating the curvature at the interface, the upper bound of the temperature difference can be calculated. This can be done by assuming the curvature κ <<1 in (10.2).

Heat transfer and fluid flow along the pipe are assumed to be one-dimensional. This is valid if the axial variation of temperature, pressure, evaporation rate, and volume flow rate occurs in a length scale that is large compared with R_p. Thus, it is necessary that the boundary layer thickness $S^{-1}L>>R_p$ or $S<<L/R_p$. This fixes an upper bound on S for our boundary-layer results to be valid.

It can also be observed that for high H and S, and H>>S, the Nusselt number approaches the values of S.

Finally, the comparison with the experimental values were pretty close. There were small errors due to some assumptions in the analysis of the heat pipe. While calculating the porosity, the bi-pyramid section that occurs between the capillaries and the pores were counted twice. This is a very small volume compared to the overall volume of the channels, hence, it was ignored.

Also, the experiments have an entire region, evaporator region for heat supplied and condenser region for heat removed. However, our model assumes the heat addition and heat removal at the edge of the heat pipe in a cross sectional plane. The temperature is increased in the

hot end and decreased in the cold end, instead of supplying heat through a section of the pipe. It is observed that this modification does not affect the result much.

CHAPTER 16. CONCLUSIONS

Heat and mass transfer has been studied for a cylindrical heat pipe with idealized porous lining. Our model incorporates evaporation and condensation kinetics, which allows calculation of liquid and vapor pressures throughout the pipe. We find that the heat transfer performance of the heat pipe depends on two dimensionless parameters: the heat pipe number H, and the evaporation exponent S. This is the first time that these dimensionless parameters have been derived for heat pipes. Analytic solutions have been obtained for the pipe temperature T_p^*, vapor pressure p_g^*, evaporation rate M^*, and other variables. We systematically investigated the effects of H and S on these variables. We can optimize the vapor heat transfer in the heat pipe for the first time because our model captures the essential physics. For fixed pipe cross-sectional dimensions, we find an optimal pipe length, and for fixed pipe length, we find an optimal wick thickness. We compute the Nusselt number for the published experiments and found good agreement without any adjustable parameters.

REFERENCES

A. Akbarzadeh, T. Wadowski, "Heat Pipe Based Cooling Systems for Photovoltaic Cells Under Concentrated Solar Radiation," *Applied Thermal Engineering.* **16**, 1 (1996)

A. Bejan, *Advanced Engineering Thermodynamics, Second ed.,* John Wiley & Sons Inc. (New York) (1997)

A. Faghri, *Heat Pipe Science and Technology*, Taylor & Francis Inc. (1995)

A. Faghri, "Review and Advances in Heat Pipe Science and Technology," *J. of Heat Transfer*. **134**, 12 (2012)

A. Faghri, "Heat Pipes: Review, Opportunities and Challenges," *Frontiers in Heat Pipes.* **5**, 1 (2014)

A. Kaw, N. Collier, M. Keteltas, J. Paul, G. Besterfield. "Holistic but customized resources for a course in numerical methods." *Computer Applications in Engineering Education.* **11**, 4 (2003)

D.C. Lu, "Fabrication and Performance Analysis of Variable Conductance Heat Pipes," *Report to National Science Council,* National Chiao-Tung University. (1995)

D. J. Struik, *A Source Book in Mathematics 1200-1800*, Harvard University Press. (Massachusetts) (1969)

D. Reay, R. McGlen, P. Kew, *Heat pipes: theory, design and applications*, Butterworth-Heinemann. (2013)

G. P. Peterson, *An Introduction to Heat Pipes,* John Wiley & Sons Inc. (New York) (1994)

H. Bandopadhayay, A. Salt, A. Siggins, A. Williams, "A Compact Heat Exchanger for Cooling of Electronic Cabinets in Locations with Very High Relative Humidity," *8th International Heat Pipe Conference,* International Academic Publishers, Beijing. (1992)

H. Wong, S. Morris, C. J. Radke, "Two-dimensional menisci in nonaxisymmetric capillaries," *J. Colloid Interface Sci*. **148**, 1: 284-287 (1992)

H. Wong, S. Morris, C. J. Radke, "Three-dimensional menisci in polygonal capillaries," *J. Colloid Interface Sci*. **148**: 317-336 (1992)

J. Andrews, A. Akbarzadeh, I. Sauciuc, *Heat Pipe Technology: Theory Applications and Prospects,* Elsevier Science, Inc. (New York) (1997)

J. Barrett, C. Clement, "Kinetic evaporation and condensation rates and their coefficients," *J. Colloid Interf. Sci*. **150**: 352-364 (1992)

J. E. Kemme, “Ultimate Heat-Pipe Performance,” *IEEE Transactions on Electron Devices*, **16.8**: 717-723 (1969)

J. G. Speight, *Lange’s handbook of chemistry*, Vol. 1. McGraw-Hill. (New York) (2005)

J. K. Fink, L. Leibowitz, *Thermodynamic and transport properties of sodium liquid and vapor*, No. ANL/RE—95/2. Argonne National Lab. (Illinois) (1995)

J. M. Tournier, M. S. El-Genk, “A Transient Analysis of Water Heat Pipe,” *ASME Winter Annual Meeting*. (New Orleans) (1993)

J. Zhang, S. J. Watson, H. Wong, “Fluid flow and heat transfer in a dual-wet micro heat pipe,” *J. Fluid Mech.* **589:** 1-31 (2007)

M. Iwasa, T. Baba, Y. Kobayashi, “Evaporation Heat Transfer Characteristics of Groove Heat Pipe,” *Symposium of Flight Mechanics and Astrodynamics*, 115-118. (1994)

M. L. Ramires, “Standard reference data for the thermal conductivity of water,” *J. of Physical and Chemical Reference Data*. **24.3**: 1377-1381 (1995)

M. Mochizuki, K. Mashiko, K. Eguchi, T. Namiki, M. Shiraishi, “Development of Large Heat Pipe for Extracting Geothermal Energy, *Symposium on Flight Mechanics and Astrodynamics*. 107-110 (1994)

M. Mochizuki, Y. Saito, H. Imura, “Cooling of Electric Power Cable by Forced Convection Two-Phase Loop Heat Pipe,” *Symposium on Flight Mechanics and Astrodynamics*. 103-104 (1994)

P. D. Dunn, D. A. Reay, *Heat Pipes*, Pergamon Press. (Oxford) (1976)

P. Xiao, P. Johnson, A. Akbarzadeh, “Application of Heat Pipe Heat Exchangers to Humidity Control in Air Conditioning Systems,” *International symposium on Energy, Environment and Economics*. (1995)

S. S. Rao, H. Wong, “Heat and mass transfer in polygonal micro heat pipes under small imposed temperature differences,” *International Journal of Heat and Mass Transfer*. **89**: 1369-1385 (2015)

S. Toyokawa, T. Araki, Y. Kobayashi, “Evaporate Heat Transfer from Edge of Liquid Meniscus in Groove Heat Pipe,” *Symposium on Flight Mechanics and Astrodynamics*. 13-23 (1993)

S. W. Chi, *Heat Pipe Theory and Practice*, Hemisphere Publishing Corporation. (Washington, D. C.) (1976)

S. Whitaker, *Flow in a porous media I: A theoretical derivation of Darcy’s law*, Transport in Porous Media. **1**: 3-25 (1986)

W. Kenneth, “Generalized Thermodynamic Relationships,” *Thermodynamics* (5th ed.), McGraw-Hill, Inc. (New York) (1988)

W. R. Lin, “Analytical Modelling of the Heat Pipe Performance and Wick Limit,” *Masters Thesis,* National Taiwan University. *(1992)*

Y. Kanesashi, H. Nishikata, M. Mochizuki, “Utilization on Exhaust Heat of Automobile Engine by Heat Pipe,” *Journal of The Japan Association for Heat Pipe.* **15**, 3: 29-32 (1996)

APPENDIX

Table A. Evaporation Number

Table A. below shows the evaporation number for water at different temperature for the Radius of pore of 1 μm.

Temperature (T_p) (K)	Density (ρ_e) (kg/m^3)	Thermal Conductivity (k_f) (W/mK)	c (s/m)	Evaporation Number (E)
273	916.2	.56	$1.12*10^{-3}$	33980
303	995.7	.61	$1.07*10^{-3}$	29180
323	988	.64	$1.03*10^{-3}$	24920
343	978	.65	$1.00*10^{-3}$	22210
363	965	.66	$9.75*10^{-4}$	19880

Table A. Evaporation number for water at different temperatures and R_p = 1 μm

The latent heat of vaporization is taken to be 2250 KJ/kg, the specific gas constant is 461.5 J/(kg.K), and the accommodation coefficient is 1. The values of thermal conductivity are taken from the experimental results by Ramires, Maria L. V (Ramires 1995).

APPENDIX A. LEADING ORDER OUTER SOLUTION

The outer region temperature can be expanded as

$$T = t_0 + \frac{1}{E} t_1 + \ldots \tag{A.1}$$

The zero-order outer solution $\bar{t}_0$ is governed by the following equation

$$\frac{1}{r_p^*} \frac{\partial}{\partial r_p^*} r_p^* \frac{\partial t_0}{\partial r_p^*} + \frac{\partial^2 t_0}{\partial z_p^{*2}} = 0 \tag{A.2}$$

At the center of the pore $r_p^*=0$,

$$\frac{\partial t_0}{\partial r_p^*} = 0 \tag{A.3a}$$

At the wall of the pore $r_p^*=1$,

$$t_0 = 1 \tag{A.3b}$$

At the interface $z_p^*=0$,

$$t_0 = 0 \tag{A.3c}$$

Finally, as $z_p^* \to \infty$,

$$t_0 \to 1 \tag{A.3d}$$

For simpler calculation purposes we define $t_0 = 1 - \bar{t}_0$ and change the boundary conditions accordingly and solve for t_0. The solution for t_0 is

$$\bar{t}_0 = \sum_{n=1}^{\infty} \beta_n e^{-\sqrt{\lambda_n} z_p^*} J_0(\sqrt{\lambda_n} r_p^*) \tag{A.4}$$

Here λ_n are the roots of zero order Bessel function of the first kind (J_0) and β_n satisfy the following equation

$$1 = \sum_{n=1}^{\infty} \beta_n J_0(\sqrt{\lambda_n} r_p^*) \tag{A.5}$$

Using the orthogonal property of Bessel functions in equation (A.5), β_n can be calculated as

$$\beta_n = \frac{2}{J_1^2(\sqrt{\lambda_n})} \int_0^1 r_p^* J_0(\sqrt{\lambda_n} r_p^*) dr_p^* \tag{A.6}$$

Here, J_1 is the first order Bessel function of the first kind.

APPENDIX B. MATLAB CODES

B.1. Dimensionless evaporation rate along the pipe for various H and S=1

```
clc
close all;
clear all;
S=1;       %S=1
H=0.01;
figure();
y=0;
n=0.0001;
while H<=10^2
  a=0;
  y=y+1;
  for x = 1:(1/n)+1
     Z(x)=a;
     M(x,y)=(((1+H)*sinh((S*(1-Z(x)))))/((S+H*tanh(S))*cosh(S)));
     a=a+n;
  end
  H=H*10;

end
plot(Z,M);
axis([0,1,0,1]);
xlabel('z^{*}')
ylabel('M^{*}')
legend('H=.01','H=.1','H=1','H=10','H=10^{2}, H=10^{3}')
title('S=1')
```

B.2. Dimensionless evaporation rate along the pipe for various H and S=100

```
clc
close all;
clear all;
S=100;       %S=100
H=0.1;
figure();
y=0;
n=0.0001;
while H<=10^4
  a=0;
  y=y+1;
  for x = 1:(1/n)+1
     Z(x)=a;
     M(x,y)=(((1+H)*sinh((S*(1-Z(x)))))/((S+H*tanh(S))*cosh(S)));
     a=a+n;
  end
  H=H*10;

end
plot(Z,M);
axis([0,.1,0,1]);
xlabel('z^{*}')
ylabel('M^{*}')
legend('H=.1','H=1','H=10','H=10^{2}','H=10^{3}','10^{4},10^{5}')
title('S=100')
```

B.3. Nusselt Number versus H for various S

```
Ss=.1;
yy=0;
n=.02;
while Ss<=10^3
   aa=1;
   yy=yy+1;
   Hh=10^-2;
   while Hh<=10^6
      Nu(aa,yy)=(1+Hh)/(1+(Hh*(tanh(Ss)))/Ss);
      HHH(aa)=Hh;
      aa=aa+1;
      Hh=Hh*2;
   end
   Hh=10^6;
   Nu(aa,yy)=(1+Hh)/(1+(Hh*(tanh(Ss)))/Ss);
   HHH(aa)=Hh;
   Ss=Ss*10;
end
figure;
loglog(HHH,Nu)
xlabel('H')
ylabel('Nu')
legend('S=1','S=10','S=10^{2}','S=10^{3}')
```

B.4. Dimensionless temperature along the pipe for various H and S=1

```
clc
close all;
clear all;
S=1;       %S=1
H=0.01;
figure();
y=0;
n=0.0001;
while H<=10^2
   a=0;
   y=y+1;
   for x = 1:(1/n)+1
      Z(x)=a;
      T(x,y)=(S/(S+H*tanh(S)))*((1-Z(x))+(((H*sinh(S ...
            *(1- Z(x))))/(S*cosh(S)))));
    a=a+n;
   end
   H=H*10;

end
plot(Z,M);
xlabel('z^{*}')
ylabel('M^{*}')
legend('H=.01','H=.1','H=1','H=10','H=10^{2}, H=10^{3}')
title('S=1')
```

B.5. Dimensionless temperature along the pipe for various H and S=100

```
clc
close all;
clear all;
S=100;       %S=100
H=0.1;
figure();
y=0;
n=0.0001;
while H<=10^4
   a=0;
   y=y+1;
   for x = 1:(1/n)+1
      Z(x)=a;
      T(x,y)=(S/(S+H*tanh(S)))*((1-Z(x))+(((H*sinh(S ...
      *(1-Z(x))))/(S*cosh(S)))));
      a=a+n;
   end
   H=H*10;

end
plot(Z,T);
%axis([0,.1,0,1]);
xlabel('z^{*}')
ylabel('T^{*}_{p}')
legend('H=.1','H=1','H=10','H=10^{2}','H=10^{3}','10^{4},10^{5}')
title('S=100')
```

B.6. Dimensionless vapor pressure along the pipe for various H and S=1

```
clc
close all;
clear all;
S=1;       %S=1
H=0.01;
y=0;
n=0.0001;
while H<=10^3
   a=0;
   y=y+1;
   for x = 1:(1/n)+1
      Z(x)=a;
      P(x,y)=(S/(S+H*tanh(S)))*((1-Z(x))-(sinh(S*((1-Z(x)))))/(S*cosh(S)));
      a=a+n;
   end
   H=H*10;

end
figure;
plot(Z,P);
axis([0,1,0,.25]);
xlabel('z^{*}')
ylabel('P_{g}^{*}')
legend('H=.01','H=.1','H=1','H=10','H=10^{2}','10^{3}')
title('S=1')
```

B.7. Dimensionless vapor pressure along the pipe for various H and S=100

```
clc
close all;
clear all;
S=100;       %S=100
H=0.1;
figure();
y=0;
n=0.0001;
while H<=10^4
  a=0;
  y=y+1;
  for x = 1:(1/n)+1
    Z(x)=a;
    P(x,y)=(S/(S+H*tanh(S)))*((1-Z(x))-(sinh(S*((1-Z(x)))))/(S*cosh(S)));
    a=a+n;
  end
  H=H*10;

end
plot(Z,P);
axis([0,1,0,1]);
xlabel('z^{*}')
ylabel('P_{g}^{*}')
legend('H=.1','H=1','H=10','H=10^{2}','H=10^{3}','10^{4}')
title('S=100')
```

B.8. Dimensionless vapor volume flow rate along the pipe for various H and S=1

```
clc
close all;
clear all;
S=1;       %S=1
H=0.01;
y=0;
n=0.0001;
while H<=10^2
   a=0;
   y=y+1;
   for x = 1:(1/n)+1
      Z(x)=a;
       V(x,y)=((1+H)/(S*(S+H*tanh(S))))*(1-(cosh(S*((1-Z(x))))/(cosh(S))));
      a=a+n;
   end
   H=H*10;

end
figure;
plot(Z,V);
axis([0,1,0,.6]);
xlabel('z^{*}')
ylabel('V_{g}^{*}')
title('S=1')
```

B.9. Dimensionless vapor volume flow rate along the pipe for various H and S=100

```
clc
close all;
clear all;
S=100;       %S=100
H=0.1;
figure();
y=0;
n=0.0001;
while H<=10^5
  a=0;
  y=y+1;
  for x = 1:(1/n)+1
    Z(x)=a;
    V(x,y)=(1+H)/(S*(S+H*tanh(S))))*((1-((cosh(S*((1-Z(x))))/(cosh(S)))));
    a=a+n;
  end
  H=H*10;
end
plot(Z,V);
axis([0,.1,0,.02]);
xlabel('z^{*}')
ylabel('V_{g}^{*}')
title('S=100')
```

B.10. Optimum pipe length S_m versus H

```
clc
close all
clear all
d=10^-4;
for i=1:11
a=0;
b=2000;
tol=1e-5;
fa=(a-tanh(a))^2-(1+d)*((tanh(a)^2)-a^2*(sech(a)^2));
fb=(b-tanh(b))^2-(1+d)*((tanh(b)^2)-b^2*(sech(b)^2));
while abs(b-a)>tol
   c=(a+b)/2;
   fc=(c-tanh(c))^2-(1+d)*((tanh(c)^2)-c^2*(sech(c)^2));
   if fa*fc<0
      b=c;
      fb=fc;
   elseif fb*fc<0
      a=c;
      fa=fc;
   else
      b=c;
   end
end
H(i)=d;
S(i)=c;
d=d*10;
end
loglog(H,S);
axis([10^-4 10^6 10^0 1.5*10^3]);
hold on
d=10^-4;
for i=1:6
   Sa(i)=1+(1+d)^(1/2);
   Ha(i)=d;
   d=d*100;
end
loglog(Ha,Sa,'*');
legend('Numerical','Asymptotic');
xlabel('H');
ylabel('S_{m}');
```

B.11. Dimensionless vapor flow heat rate versus S for various H

```
clc
close all
clear all
H=0.1;
v=-2:2:10;
for i=1:8
   m=-4;
   for j=1:800
      S(j)=10^m;
      q(j)=(H*(S(j)-tanh(S(j))))/(S(j)*(S(j)+H*tanh(S(j))));
      m=m+2/100;
   end
   semilogx(S,q)
   axis([10^-3,10^10,0,1]);
   xlabel('S')
   ylabel('q_{v}^{*}')
   set(gca, 'XTick', 10.^v)
   hold on
   H=H*10;
end
legend('H=.1','H=1','H=10','H=10^{2}','H=10^{3}',...
      'H=10^{4}','H=10^{5}','H=10^{6}')
```

B.12. H, S and $\bar{q}_v$ versus R_g^* for various H_w

```
clc
close all
clear
Rp=0.0001;
Ro=1.2;
Hw=10;
kf=0.1;
ks=1;
N=0.1;
L=20;
Mp=0.01;
Re=10^4;
qv=zeros(100,8);
S=zeros(100,8);
H=zeros(100,8);
SkA=zeros(100,8);
rg=zeros(100,8);
for b=1:8
   a=1;
   for x=0.01:0.01:1
      rg(a,b)=x;
      SkA(a,b)=(kf*N^2*(1-rg(a,b)^2)+ks*(1-rg(a,b)^2)*(1-pi*N^2)+(Ro^2-1));
      H(a,b)=1/8*(Hw*rg(a,b)^4)/(SkA(a,b));
      S(a,b)=((16*pi*N^2/Rp*(1+rg(a,b))*Mp/(Re*rg(a,b)^4))*(H(a,b)+1))^(1/2)*L;
      qv(a,b)=(((1+H(a,b))/(1+H(a,b)*tanh(S(a,b))/S(a,b)))-1)*(SkA(a,b)/((Ro^2-1)));
      a=a+1;
   end
   Hw=Hw*10;
end
plot(rg,qv);
ylabel('q_{v}^{*}')
xlabel('R_{g}^{*}')
figure;
plot(rg,S);
ylabel('S')
xlabel('R_{g}^{*}')
figure;
plot(rg,H);
ylabel('H')
xlabel('R_{g}^{*}')
```

B.13. S and $\bar{q}_v$ versus R_g^* for various N^*

```
clc
close all
clear
Rp=0.0001;
Ro=1.2;
Hw=10^7;
kf=0.1;
ks=1;
N=0.1;
L=10;
Mp=0.01;
Re=10^4;
qv=zeros(100,3);
S=zeros(100,3);
H=zeros(100,3);
SkA=zeros(100,3);
rg=zeros(100,3);
for b=1:3
   a=1;
   for x=0.01:0.01:1
      rg(a,b)=x;
      SkA(a,b)=(kf*N^2*(1-rg(a,b)^2)+ks*(1-rg(a,b)^2)*(1-pi*N^2)+(Ro^2-1));
      H(a,b)=1/8*(Hw*rg(a,b)^4)/(SkA(a,b));
      S(a,b)=((16*pi*N^2/Rp*(1+rg(a,b))*Mp/(Re*rg(a,b)^4))*(H(a,b)+1))^(1/2)*L;
      qv(a,b)=(((1+H(a,b))/(1+H(a,b)*tanh(S(a,b))/S(a,b)))-1)*(SkA(a,b)/((Ro^2-1)));
      a=a+1;
   end
   L=L*10;
end
plot(rg,qv);
ylabel('q_{v}^{*}')
xlabel('R_{g}^{*}')
figure;
plot(rg,S);
ylabel('S')
xlabel('R_{g}^{*}')
```

B.14. H, S and $\bar{q}_v$ versus R_g^* for various N^*

```
clc
close all
clear
Rp=0.0001;
Ro=1.2;
Hw=10^7;
kf=0.1;
ks=1;
N=0.01;
L=20;
Mp=0.01;
Re=10^4;
qv=zeros(100,4);
S=zeros(100,4);
H=zeros(100,4);
SkA=zeros(100,4);
rg=zeros(100,4);
for b=1:4
   a=1;
   for x=0.01:0.01:1
      rg(a,b)=x;
      SkA(a,b)=(kf*N^2*(1-rg(a,b)^2)+ks*(1-rg(a,b)^2)*(1-pi*N^2)+(Ro^2-1));
      H(a,b)=1/8*(Hw*rg(a,b)^4)/(SkA(a,b));
      S(a,b)=((16*pi*N^2/Rp*(1+rg(a,b))*Mp/(Re*rg(a,b)^4))*(H(a,b)+1))^(1/2)*L;
      qv(a,b)=(((1+H(a,b))/(1+H(a,b)*tanh(S(a,b))/S(a,b)))-1)*(SkA(a,b)/((Ro^2-1)));
      a=a+1;
   end
   N=N*2.5;
end
plot(rg,qv);
ylabel('q_{v}^{*}')
xlabel('R_{g}^{*}')
figure;
plot(rg,S);
ylabel('S')
xlabel('R_{g}^{*}')
figure;
plot(rg,H);
ylabel('H')
xlabel('R_{g}^{*}')
```

VITA

The author, Pramesh Regmi, was born in Lalitpur, Nepal in October 1992. He graduated from Rato Bangala School in 2010.

In August 2011, he joined McNeese State University (Lake Charles, Louisiana) for Bachelor of Science in Mechanical Engineering. He obtained his degree in May 2015 with a summa cum laude honor. While at McNeese, he published a paper in "Numerical and Experimental Investigation of Heat Transfer Coefficient and Friction Factor in Internal Channels With Fins" during the Joint ASME/JSME/KSME Conference, 2015.

In August 2015, the author joined Louisiana State University (LSU) for Master's degree in the Department of Mechanical Engineering. He is expected to graduate in May 2017.